Analysis and prediction of the brain deformation during a neurosurgical procedure

Author :
Olivier Clatz
DEA Mathematiques Vision Apprentissage
ENS Cachan

Advisor :
Nicholas Ayache. Scientific Leader.
Herve Delingette. Principal research scientist.
Eric Bardinet. Expert Engineer.

École Normale Supérieure de Cachan
61, avenue du Président-Wilson
94235 CACHAN Cedex
FRANCE

EPIDAURE, INRIA
2004 route des Lucioles BP 93
06902 SOPHIA ANTIPOLIS Cedex
FRANCE

Analysis of the brain deformation during a neurosurgery operation

Abstract: The goal of this 5 months internship was to develop a realistic biomechanical model of the brain to predict intra operative deformation (the brain shift phenomenon). Such a model would be very useful to update the pre-operative surgical planning and help the surgeon to avoid interfering with critical organs, by balancing the deformation effects of the skull aperture visible on the post-operative MRI.

We have, in a first stage, compared pre and post-operative MRI with a non rigid registration software. In a second stage, we have proposed a biomechanical volumetric model which could explain the measured deformations. The objective was to create a parametrical model that both relates the prediction to the post operative MRI and takes account of the anatomy. To solve this problem, we had to solve a reverse problem : what are the physical parameters of the cerebral parenchyma as well as external forces that accounts of the displacement computed by non rigid registration.

Key-words: Brain shift, biomechanical models, intraoperative deformation, linear elasticity, medical imaging.

Analyse et prédiction de la déformation per-opératoire du cerveau au cours d'une intervention en neuro-chirurgie

Résumé: L'objectif de ce stage etait de modéliser et de prédire la déformation du cerveau (appelée "brain-shift" en anglais) lors d' une intervention en neuro-chirurgie. Une telle modélisation servirait à la mise à jour du planing pré-opératoire (permettant d'éviter de toucher certaines structures vitales) pendant l'intervention, en compensant les effets mécaniques liés à l'ouverture de la boîte crânienne.

Nous avons dans un premier temps comparé des images IRM post-opératoires et per-opératoires du cerveau à l'aide d'un outil de recalage non rigide. Nous avons ensuite proposé un modèle volumique puis un modèle biomécanique du cerveau. Ce modèle biomécanique repose sur des lois de comportement ainsi que des conditions aux limites représentatives de l'etat du cerveau pendant un acte neurochirurgical. Afin de comprendre et de modéliser cette déformation, nous avons cherché à résoudre un problème inverse : quels sont les paramètres physiques du parenchyme cérébral ainsi que les forces appliquées permettant d'expliquer la déformation mesurée par l'outil de recalage.

Mots Clés: Déformation per-opératoire, modèles biomécaniques, élasticité linéaire, pneumocéphalus, imagerie médiacle.

Acknowledgments

First of all, I would like to thank Prof Ayache and Dr Delingette for welcoming me in the EPIDAURE project and offering me the chance to work in the best conditions on such an exciting subject. Besides the numerous remarks and discussions, their outstanding support while supervising this internship significantly contributed to this dissertation.

I would also like to thank Eric Bardinet and Stéphane Litrico for the valuable discussions we had together. Additionally, many thanks to Maxime Sermesant and Clément Forest for their availability and their useful help. Then, I would like to acknowledge Drs. Ron Kikinis, Martha Shenton, Robert McCarley, and Ferenc Jolesz for sharing the digital brain atlas.

Lastly, I would like to to thank my family, my friends, and all those who supported me during the past 5 months.

Contents

Chapter 1

Introduction

1.1 EPIDAURE research project

The aim of the project is the development of new tools in Medical Imaging and Robotics. The studied images are anatomical and functional images from : conventional radiology imagery, X-Ray Computed Tomography (CT),Magnetic Resonance Imaging (anatomical, functional and angiographic MRI), Isotopic Imaging (Spect and PET), Ultrasound Imaging, Histology Imaging, Monocular or Stereoscopic Video Imaging.

Among the main research themes of the team, one can find the extraction of quantitative parameters (shape, texture) from images, image registration (temporal, multi-modal, multi-subject...), the construction of anatomical and functional atlases from images, morphometry (statistics on shape and intensities), the analysis of the cardiac motion, modeling of soft tissues for visual and haptic interaction, physiological models of organs, and the coupling of medical imaging and robotics.

Application domains are :

- computer aided diagnosis
- surgery simulation (which can imply virtual reality and robotics tools)
- image guided therapy (planning, control and follow-up)
- augmented reality and robotics tools

1.2 Context of this work

During the past decades, importance of medical image processing and analysis have increased so as to become a discipline of its own. The reason for this incredible development comes from the new possibility of acquiring 3D information on invisible anatomy below the skin. This significant technological improvement deeply changed the diagnosis and the treatment of abnormalities. Among the numerous applications of these new technologies, those related to brain radically transformed the entire surgical procedure. The pre-operative planning precision increased with the image quality, allowing to operate on new diseases, like the Parkinson one. In addition to the pre-operative image, in the case of tumor resection, neuro-navigation helps the surgeon to accurately determine lesions localization.

The principal problem with pre-operative planning as well as image guided neuro-navigation is the assumption that anatomical structures do not move between the imaging time and the operation time. In reality, positions and shape of the brain tissue change with time during the operation and significantly decrease the accuracy of the planning made on the pre-operative image. The ideal solution would be to have per-operative image to register pre-operative images (and planning) with per-operative images. To solve this problem, technological solution exists like open-configuration magnetic resonance scanners. In this case, the operative room entirely consists of equipment safe to use around a 0.5T magnetic field (figure 1.1). However this kind of scanner and adapted equipment is too expensive to supply each surgeon's demand. Alternative solutions have been proposed, like using Ultra Sound devices during the operation. However up-to-now, they provide images of poor quality and do not really give satisfaction.

Figure 1.1: Intraoperative magnetic resonance imaging scanner of the Brigham and Women's Hospital in Boston. (http://www.boston-neurosurg.org/)

To reduce the effect of intraoperative deformations, we propose in this report a new biomedical model of the human head, able to take account of the patient specificity to predict the brain shift phenomenon during the operation. We will, in this first study, focus on the effect of gravity on the brain deformation after the dura-mater opening.

The main contributions of this work are :

- An new biomechanical static model with an explicit link between the brain shift phenomenon ,CSF leak and CSF liquid level in the skull.
- The use of a non rigid software to evaluate the quality of the prediction.
- A model which takes account of the asymmetry of the measured displacement field.

1.3 Organization of the text

In order to develop this dissertation on the creation of a new biomechanical model of the human head, we have decomposed this text in three main parts. The first one (chapter 2) starts with the state of the art. The second one (chapters 3-5) deals with the image analysis. The third one (chapters 6-7) develops the mechanical model. The document ends with the conclusion and perspectives.

- **Chapter 2** presents a general overview of the existing literature dealing with parametric models of the head, classified in three categories. The first one uses per-operative information to register a model based on the pre-operative image. The second one compares the model comportment with in vivo experiments. The third uses the model for predictive purpose.

- **Chapter 3** details the pre-processing applied on images : the two different approaches proposed to extract the cortex and the generation of the mesh based on patient anatomy.

- In **Chapter 4** we describe the non-rigid algorithm used in this study to compute displacement fields as well as the error criterion. After presenting general registration techniques, we detail the main differences between this algorithm and other non rigid registration algorithms.

- In **Chapter 5** we report on the different analysis we made on displacement fields. This analysis, computed on the displacement field and on its derivative (deformation tensor) leads to the boundary conditions applied on the biomechanical model.

- **Chapter 6** gives a summary of continuum mechanics theory, Finite Element Modeling, linear elasticity in tetrahedrons and hyperelastic material.

- **Chapter 7** presents the biomechanical predictive model. Based on our previous observations (chapter 5), we propose **displacement and force** boundary conditions to apply on the model. Prediction is compared to real deformation measured with the non rigid algorithm.

- **Chapter 8** ends by drawing the conclusion of this work and pointing out perspective for future research.

Finally the **Appendix** gives details about anatomy vocabulary used in this report.

Chapter 2

State of the art

Among the different fields of research in the modelization of brain deformation , we can distinguish three different approaches :

1. One combines pre-operative images of the patient (most common ones are MRI) with intra operative information (of different nature: ultra-sound, stereo vision, scanner ...). This information is used to register the pre-operative images and to recover deformation of brain structures.

2. One is the creation of a specific model able to recover deformations measured in traction/compression like experiments. These kind of experiments are called rheological experiments.

3. One uses a comportment model (based on statistics or biomechanics) with pre-operative images to predict the deformation in any kind of surgical procedure.

Although our approach belongs to the third group, an overview of all the different techniques used in brain deformation modeling will be very useful to build a more realistic model.

2.1 Intra-operative updated models

Bibliography in this area of research is the most important. All of the following models use intra-operative information to force displacement of structures located in the pre-operative MRI according to displacements measured during the surgical procedure. These examples combine a biomechanical model of the brain with **displacement** boundary conditions to update the pre operative MRI. One can however notice that in this condition, applied displacements have a greater influence on the deformation that material parameters.

2.1.1 Stereo vision model updated (Skrinjar [2])

The approach proposed by Skrinjar [2] uses a stereo vision reconstructed surface of the brain (figure 2.1) to update a biomechanical model in the case of epilepsy surgery. Because of the nature of the procedure (implantation of grids of electrodes under the dura-mater), significant enough surface is observed by cameras evaluate brain surface displacement.

Although his first experiments were made with a spring-mass based model, Skrinjar has used in his recent publications a continuous mechanics based model for three different reasons :

- A spring-mass based model has no real physical equivalent stiffness.
- The incompressibility constrain is difficult to model with a spring-mass based model.
- The physical comportment of the new model is closer to reality.

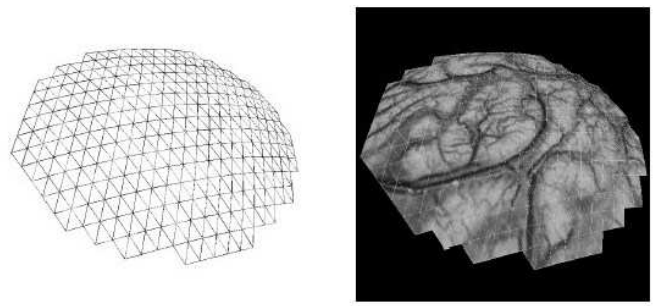

Figure 2.1: Mesh of the stereo vision extracted surface.

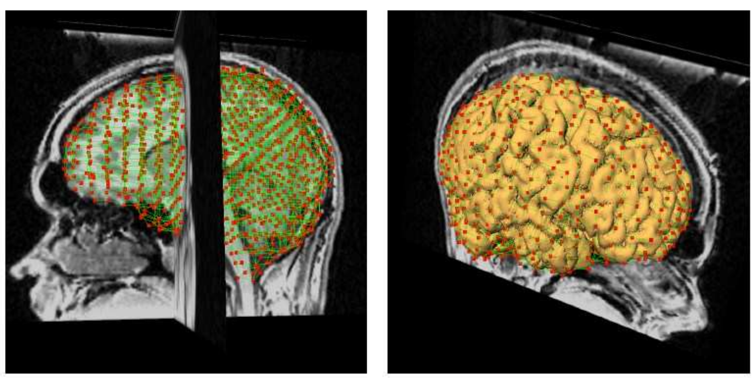

Figure 2.2: Entire brain mesh

time	0:00	7:40	14:40	19:40	24:40	34:52	49:00	max
(a)	0.34	1.38	2.21	2.30	2.74	3.24	3.29	3.29
(b)	0.34	0.45	0.30	0.13	0.20	0.32	0.04	0.45

Figure 2.3: Average displacement of the brain surface. (a: real surface displacement , b: model error)

The biomechanical model used to update the pre-operative MRI is static and damping in the mechanical equation is only used to stabilize the numerical resolution. The biomechanical model takes account of the contact with the skull by moving at each iteration each vertex which intersects the skull on its surface. The Poisson coefficient is taken equal to 0.4 for all the tissues (almost incompressible). A dichotomy like method is used to compute elasticity properties of the brain. Table 2.3 presents the computed displacement errors for the brain surface during the operation compared to the real brain surface displacement.

2.1.2 3D digitalizer model updated (Audette [4])

The approach presented in Michel Audette thesis document (http://www.bic.mni.mcgill.ca/users/maudette/homepro.html) is similar to Skrinjar's one : a biomechanical model of the brain is updated using part of the brain surface displacement information. This surface is tracked via a 3D digitalizer, composed of a rotating plane laser and a camera (fig 2.4). Except the null displacement for the brain surface at the base of the skull, the full mechanical model is not given in the thesis submission document.

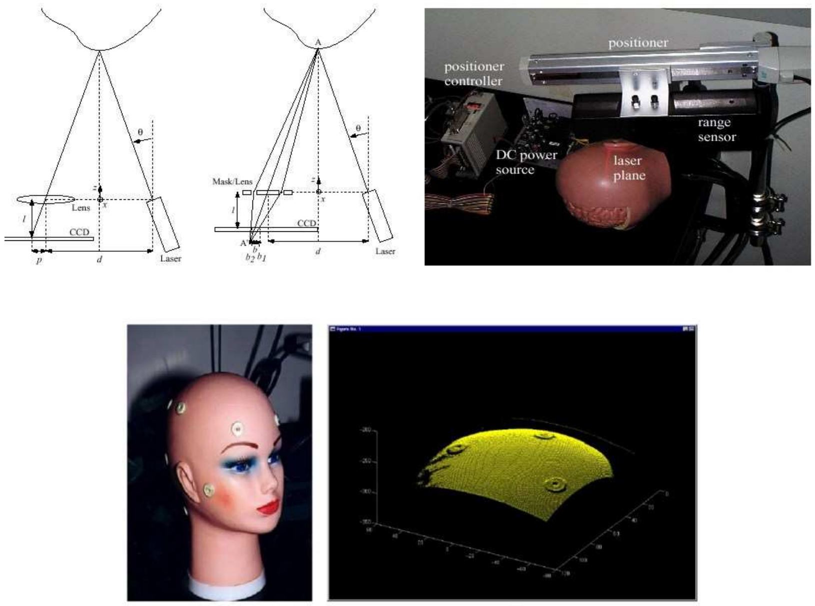

Figure 2.4: 3D digitalizer used on a phantom and reconstructed surface.[4]

2.1.3 Intra-operative MRI model updated (Ferrant [1])

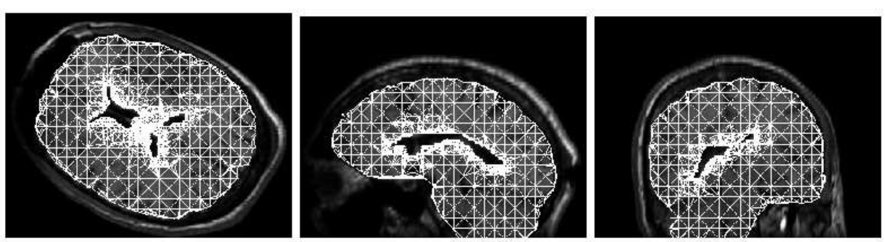

Figure 2.5: Mesh of the pre-operative MRI. One can notice elements densification around boundary surfaces [1]

The approach proposed by Matthieu Ferrant is based on intra-operative information provided by an open-configuration Magnetic Resonance Scanner. Characteristic surfaces (brain surface, ventricles) are extracted from the pre-operative MRI. A deformable model is used to make these characteristic surfaces evolve to match the per-operative surfaces. They are then used as displacement boundary conditions for a fast biomechanical

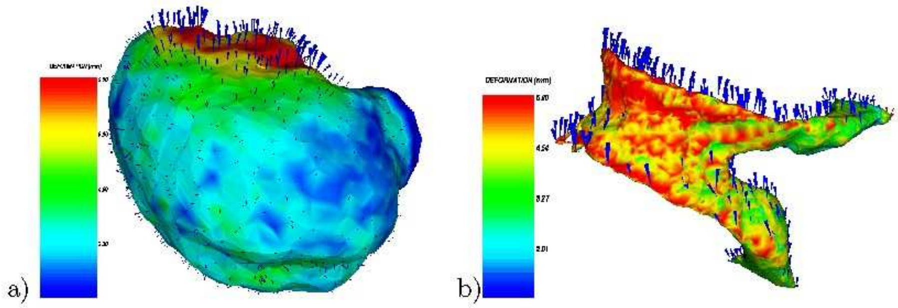

Figure 2.6: Displacement field obtained for brain and ventricles.[1]

model (fig 2.5) to recover intra-parenchymous deformation. Mechanical properties of the material are close to Skrinjar's ones : E=3KPa and ν=0.45

Although this method indisputably gives the best results of the three method presented here, the open-magnetic resonance scanner remains too expensive to be used in every hospital.

2.2 Rheological experiments

One can find in the literature lots of biomechanical experiments made on the brain. Most relevant ones in this domain are certainly the studies conducted by Karol Miller [16][17]. He has been involved into several in-vivo experiments on pig brains (figure 2.7). Based on his experiments, he has compared the bi-phasic material comportment to the (hyper)viscoelastic one [17] to find the most appropriated comportment law to relate of the brain deformation under different loads. His work shows that brain tissue can be best modelled with an homogeneous hyper-viscoelastic non-isotropic material. However, Karol Miller insists on the fact that further research still need to be done, and especially to estimate the influence of friction between brain and skull.

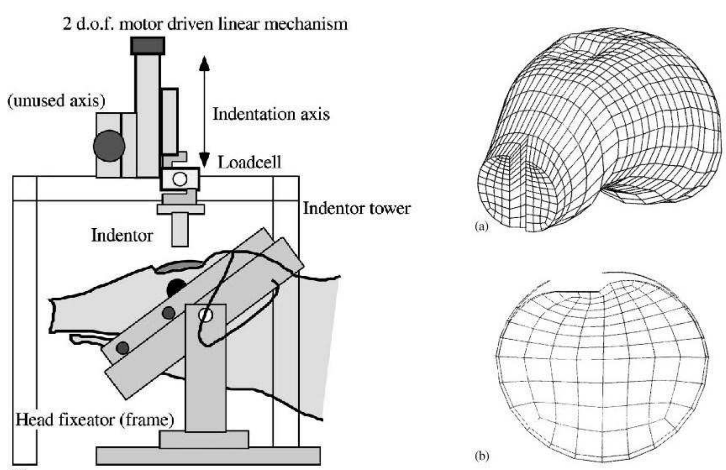

Figure 2.7: In vivo compression test on a pig brain and FEM associated.

2.3 Predictive models

2.3.1 Statistical models

Davatzikos et al propose a statistical method to estimate the relationship between brain deformation and applied forces. Due to the lack of data to make a serious survey of brain shift deformation "modes", they propose to train the model on a FEM model of the brain. This method has also the nice advantage to control the value of the applied forces leading to the observed deformation. A principal component analysis is then computed on the obtained deformed brain and only first components are used to describe deformations. Nevertheless, this method seems very limited to be used in a real surgery procedure due to the incapacity to catch each procedure specificity.

2.3.2 Biomechanical models

Miga et el. and Castellano, Hill et al. are, to our knowledge, the only ones to propose a predictive model based on biomechanics. The model proposed by Miga et al. [11, 13, 14, 20] is bi-phasic : the brain consists in a matrix full of CSF. The brain shift is then characterized by the loss of CSF in the matrix. Global parameters of the model are given in the following table :

Mesh type	Tetrahedral ~16000 vertices
Mechanical model	Finite element based on continuous mechanics
Material	CSF / air : fluid Brain : Matrix Os : rigid
Error criterion	Displacement in 4 characteristics points
Results	~30% error

Material properties :

Properties		Grey mat.	White mat	Tumor	Falx cerebri
Young modulus	Pa	2100	2100	2.1×10^4	2.1×10^5
Poisson ratio		0.45	0.45	0.45	0.45
Hydraulic cond.	$m^3.s.Kg^{-1}$	10^{-10}	10^{-12}	10^{-12}	10^{-13}
Density	$Kg.dm^{-3}$	1	1	1	1

Boundary conditions are applied on 3 different parts of the brain :

- The upper part is displacement-fixed free. The brain matrix is full of air.
- The middle part slides on the skull. The brain matrix is still full of air.
- The lower part slides on the skull. The brain matrix is full of CSF.

Geometrical position of frontiers between these three parts depends on the patient's head position and the position of the skull aperture. Error is calculated on 3 or 4 characteristic points over 4 cases (See figure 2.8 for results). Based on this error criterion, the model can account for approximately 79% of the deformation.

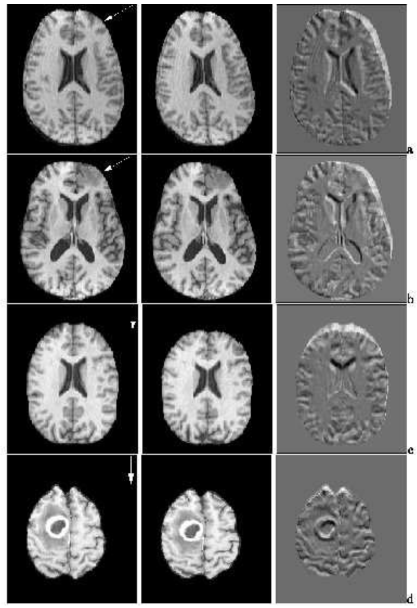

Figure 2.8: Gravity-induced brain deformation for four patients and gravity direction. Left : preoperative MRI, center: deformed image, right: difference.

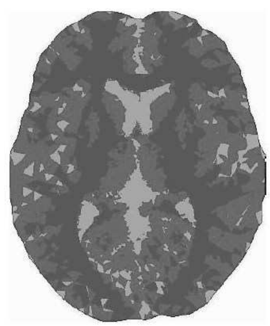

Figure 2.9: Tetrahedral mesh, Castellano, Hill et al. [6]. Different gray levels are used for different material properties

Recently Castellano, Hill et al. [18, 19] have also proposed a predictive model. An atlas-based model and mesh is firstly built (fig. 2.9) and then registered on the patient pre-operative MRI. However the model do not seem to be finalized yet. However in addition to anatomical structures, physiological constraints are planned to be taken into account for this model : CSF loss, blood pressure, drug influence evaluation...

Chapter 3

Image pre-processing

3.1 Motivation

To analyze the effect of gravity on the brain, we need to process pre and post-operative images without parenchyma resection, and more generally, find operation with as less as possible impact on the biomechanical comportment of the brain.

Among the different neurosurgery operations on the brain, Parkinson disease operation offers the advantages of presenting large brain deformations as well as not changing the mechanical integrity of the brain. The Parkinson disease renewed the interest for functional stereotactic surgery. It is a non destructive technique which consists in the deep implantation of an electrode in the brain. Patient's head is fixed to the stereotactic frame (figure 3.1). But because of the intervention duration (6 to 10 hours), a CSF leak is observed during the procedure and leads to a displacement of the brain.

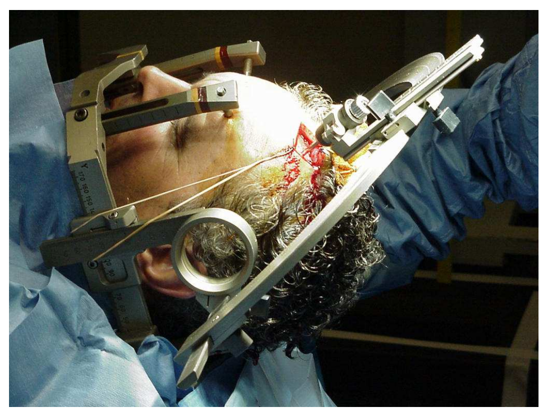

Figure 3.1: Stereotactic operation.

We have in this study used 7 cases of Parkinson operations, staggered over two years between 1999 and 2001 (figure 3.2), realised at La Pitié Salpétrière hospital (paris). The white dots on pre-operative MRIs are created by the tubes of the stereotactic frame. They are used as a fixed referential positioned on patient's head. Based on this information, surgeons decide the pre-operative planning and the two electrodes trajectory. The frame is then used during the surgical procedure to guide electrodes to the targets located on the pre-operative planning.

3.2 Cortex segmentation

As can be seen on figure 3.2, the screws of the stereotactic frame induce very important artifacts on the skull, especially because of screws introduced into the bone. In addition to these artifacts, oedemas also locally

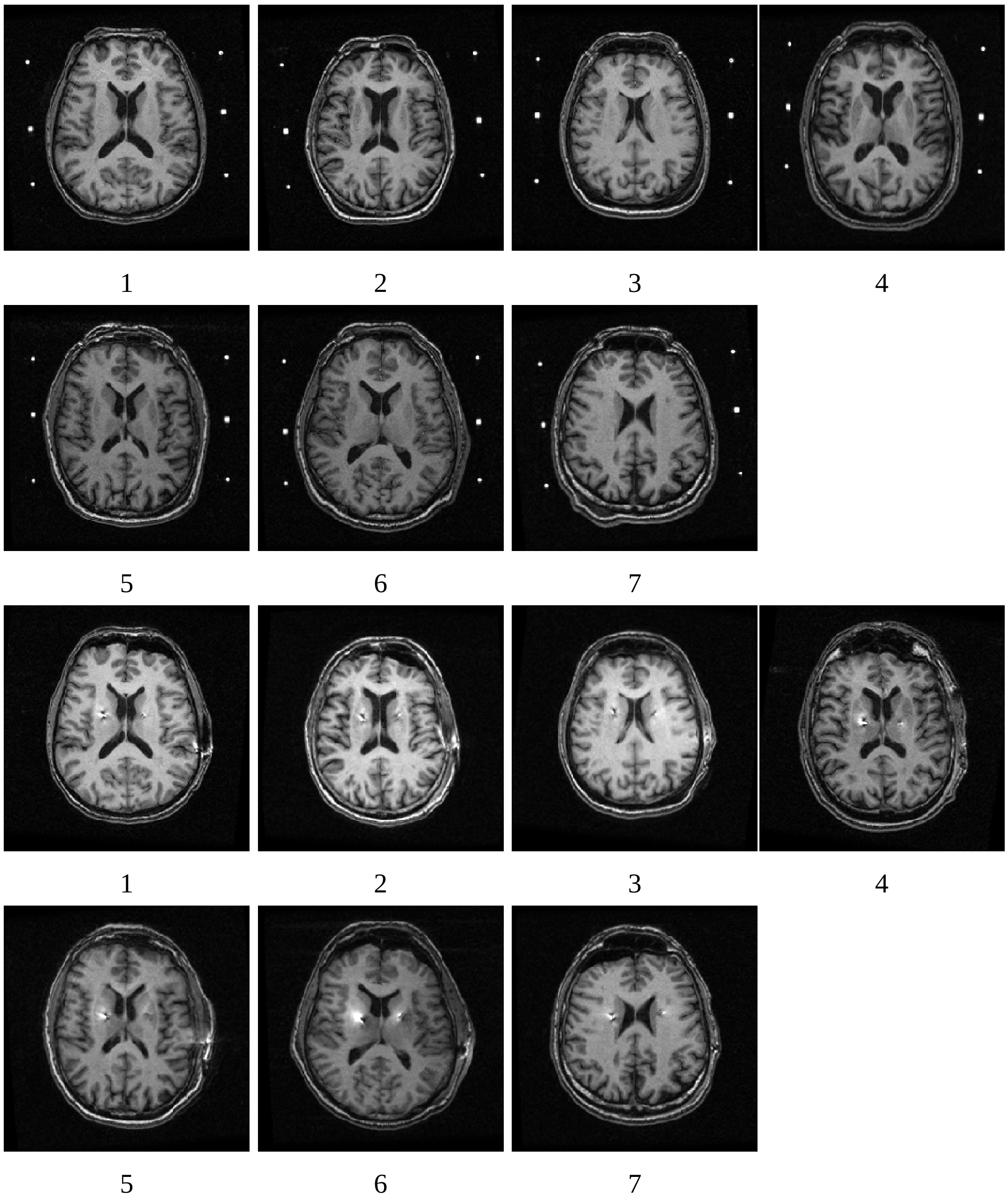

Figure 3.2: The 7 pre (top) and post (bottom) operative MRI cases used for this study.

distort skin and fat material on post-operative MRI. For these reasons, we have chosen to segment the brain on pre and post operative MRIs to study the specific deformation of the brain and reduce the effects of these different artifacts. In addition, we need to create the patient-specific mesh.

We first chose an basic approach inspired by Mangin's work [21] to segment the cortex based on morpho-mathematic operations :

threshold $\Longrightarrow$ opening $\Longrightarrow$ extraction of the largest connected components $\Longrightarrow$ closure $\Longrightarrow$ mask

Despite its good results, it requires the user to manually set a threshold and check for possible segmentation problems like the ones shown in figure 3.3 and becomes unsuited to process a large volume of MRI.

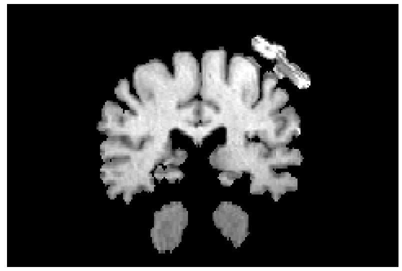

Figure 3.3: Segmentation problem encountered with the morphomathematic based method

That is why we have developed an automatic method based on the registration of a digital atlas (figure 3.4 http://splweb.bwh.harvard.edu:8000/pages/papers/atlas/text.html) on the pre/post operative MRI.

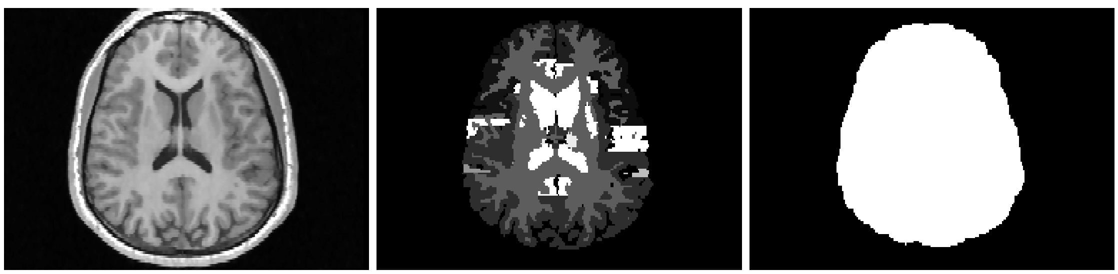

a b c

Figure 3.4: a: Atlas MRI, c: segmented structures, d: brain mask

To obtain the best precision in the registration procedure, we have split it into different stages, with increasing complexity, initializing each displacement field by the previously computed one :

$$\text{rigid} \Longrightarrow \text{similarity} \Longrightarrow \text{affine} \Longrightarrow \text{non-rigid}$$

We have used PASHA algorithm [23] for the non rigid registration and YASMINA algorithm [25] for the rest of the registration procedure. Details about the non rigid algorithm are given in chapter 3.2.

Finally, we have used the total displacement field obtained to deform the brain mask. This method offers significant advantages compared to the morphomathematic one :

- Robustness to noise and artifacts (like the electrodes' one in the post operative MRI).
- Completely automatic method.
- Preservation of dark structures (ventricles, sulci).

Our different experiments have showed that results are a little bit better with a 1 voxel dilated mask. Although this method is also less precise and often segments dura-mater, experiences show that unexpected dura-mater pieces are both segmented on the pre and post operative MRI. To balance the matching problem due to artifacts, we have used a large regularization criterion (gaussian smoothing at each iteration of the registration algorithm of 5.0). Figure 3.5 shows the segmentation results for the 7 post-operative cases. The same work has been performed on the pre-operative MRI. This last method has finally been the one employed to segment every cortex. It presents the nice advantage to also give each displacement field from the acquired MRIs to the digital brain atlas, so that it provides us the way to register each patient in the same geometry.

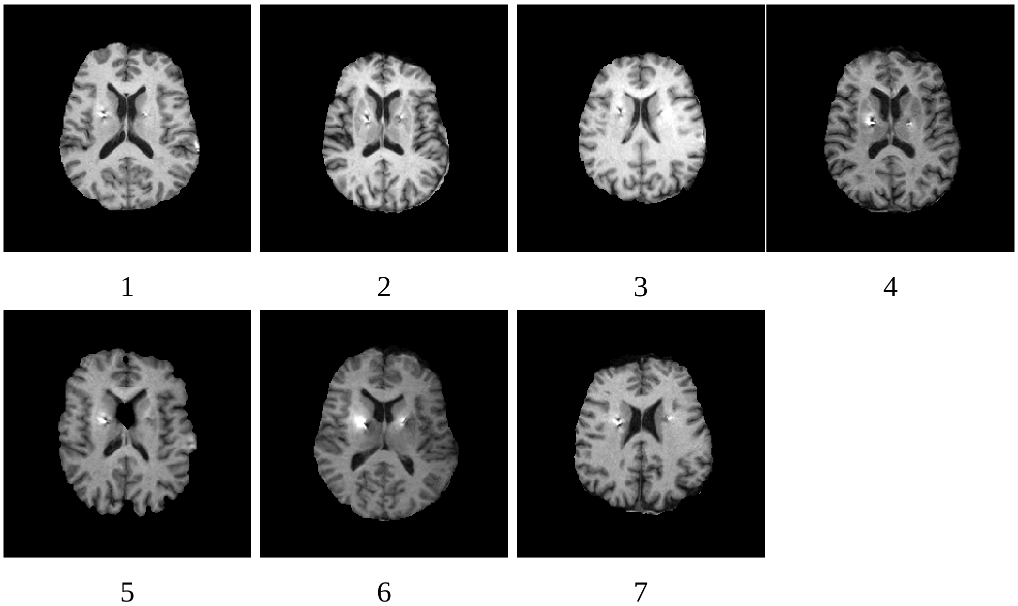

Figure 3.5: The 7 pre-operative segmented cortices.

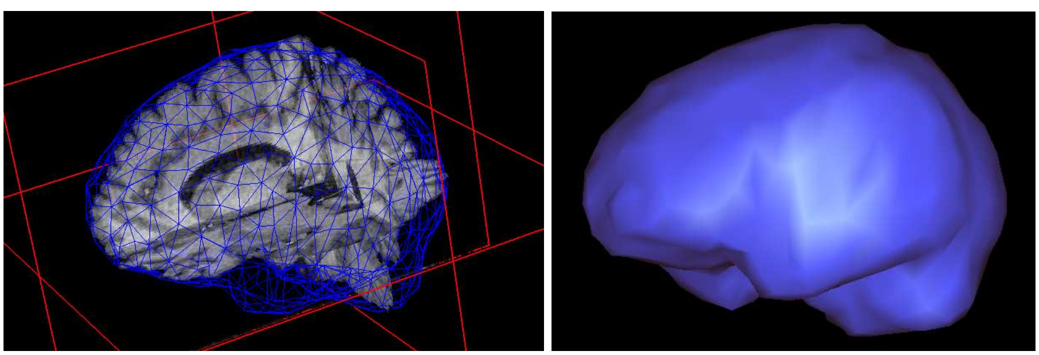

Figure 3.6: Final tetrahedral mesh of the brain

Once each brain has been segmented, we reuse their corresponding mask to generate a surface mesh of the brain of approximately 2000 triangles. We finally generate the volumetric mesh (figure 3.2) from the surfacic one with a generic software developed at INRIA Rocquencourt (GHS3D). This software minimizes the shape variability between all tetrahedrons in the final mesh so as to be optimized in tetrahedron quality point of view for mechanics treatment.

The proposed method allow us to automatically create a patient-specific mesh of the cortex.

Chapter 4

The registration algorithm

4.1 Introduction

The non rigid registration algorithm is a key point of all the remqinder. It is used to compute the displacement field between pre and post operative MRI as well as to compute an error estimation between the predicted deformation MRI. Let us briefly detail the differences between all the non-rigid registration techniques before presenting the PASHA algorithm (Cachier PhD thesis [23]) used in this following document.

Among the registration techniques, we focus more particularly on the following two major axes :

- **The regularization model** expresses the prior knowledge about the nature of the transformation.
- **The features** represent the image information used by the algorithm to guide the motion model.

4.1.1 Regularization models

It is necessary to impose in motion model to the registration algorithm, otherwise the motion of a point would be estimated independently of the motion of neighboring points, and we would thus obtain a very discontinuous displacement field. The motion model should constrain the estimated transformation using the prior knowledge about the real transformation. Therefore, the motion model greatly depends on the goal of registration: physical deformations, spatial distortions or a simple Cartesian coordinate change.

In the field of image registration, we distinguish three kind of motion models: parametric, competitive, and fluid models.

4.1.1.1 Parametric models

The parametric approach constrains the estimate T of the transformation to belong to some low dimensional transformation space $\mathcal{T}$. If $D(I,J,T)$ is some registration distance between the images I and J registered by a transformation T, a parametric approach solves the following minimization problem:

$$\min_{T \in \mathcal{T}} D(I,J,T)$$

Among the most popular choices of transformation space, we find rigid and affine groups, B-spline.

4.1.1.2 Competitive regularization

Competitive models rely on the use of a regularization energy R carrying on T. Whereas parametric regularization is a binary penalization — no transformation outside the transformation space is allowed, all the transformations inside are equiprobable — the competitive approach penalizes a transformation proportionally to its irregularity measured by the regularization energy R [27]. Competitive algorithms puts in competition D and R by solving the following problem:

$$\min_{\forall T} D(I,J,T) + R(T) \tag{4.1}$$

A popular choice of regularization energy in image registration is the energy of linear elasticity :

$$R(T) = \frac{\lambda}{2}[div(T)]^2 + \mu||dT||^2 - \frac{\mu}{2}||rot(T)||$$

4.1.1.3 Fluid regularization

Fluid models also rely on the use of a regularization energy R. This time, however, this energy does not carry on the transformation itself, but only on its *evolution*. In a discrete, or iterative, view of the process, the regularization energy measures on the difference between the current and the last estimate of the transformation: at iteration $n > 0$, the estimate T_n of the transformation is found by minimizing

$$\min_{\forall T_n} D(I,J,T_n) + R(T_n - T_{n-1})$$

4.1.2 Features

When classified according to the information used to recover the transformation T, registration algorithms are usually divided into three sections: geometric feature based (GFB) algorithms, standard intensity based (SIB) algorithms and iconic feature based (IFB) algorithms.

4.1.2.1 Geometric feature based (GFB) registration

GFB algorithms rely on a prior segmentation of the images, done generally before the registration process itself. The segmented geometrical objects correspond to anatomical or mathematical invariants, like organ boundaries or differential invariants. Once extracted from the images, these sets of points are registered using a geometrical similarity criterion. Most of the time, this similarity needs explicitly to compute a set of correspondences C between points of the two sets.

4.1.2.2 Standard intensity based (SIB) registration

Image intensities are another possible useful information for recovering the motion. The distance D between two images is then one of the many existing intensity similarity measure S, such as the sum of squared difference (SSD), the correlation coefficient (CC), the correlation ratio (CR), and the mutual information (MI) of the intensities of images I and J. Given a transformation T, the intensity similarity measure is computed between points lying at the same position; in other words, because of the density of the intensity information,

$C = T$ is implicitly done. Sébastien Ourselin's theses ([8]) is a good example of SIB in the case of rigid registration.

4.1.2.3 Iconic feature based (IFB) registration

Iconic feature based algorithms are really intermediate between the two previous categories. On one hand, as for GFB registration, we search for correspondences C between features in the images, and use a *geometric distance* to fit the transformation T to C. On the other hand, as for SIB registration, there is no segmentation of the images, as we use an intensity similarity measure to pair features.

In short, IFB algorithms pair points, lines, or regions, according to their intensity, and fit geometrically a transformation to these pairings.

4.2 The PASHA algorithm

The PASHA algorithm has been developped in the epidaure project by Pascal Cathier during his PhD [23]). Contrary to most of the IFB algorithms, which do not minimize a global energy, but firstly search for a set of correspondences and then a transformation, the PASHA algorithm proposes to minimize the following energy for iconic point feature based registration:

$$E(C,T) = S(I,J,C) + ||C-T||^2 + R(T) \tag{4.2}$$

The registration energy E depends on two variables, C and T, that are both vector fields (with one vector per pixel). C is a set of *pairings* between points: for each point of I, it gives a corresponding point in J that attracts this point. T is the estimate of the transformation: it is a smooth vector field (constrained by the regularization energy R) that is attracted by the set of correspondences C. In the energy, S is an intensity similarity measure, used to find the correspondences C, and R is a regularization energy, used to regularize T.

The energy 4.2 depends of two vector fields, C and T. One could minimize this energy with respect to C and T simultaneously. However, when the regularization energy R is quadratic, the alternate minimization w.r.t. C and T is appealing, because both partial minimizations are very fast: the minimization w.r.t. C can be done for each pixel separately most of the time, and the second step is easily solved by linear convolution. Even if the alternate minimization is known to take more iterations to converge, the overall process of minimization is relatively faster.

The algorithm, called PASHA is designed on that principle. It minimizes the energy 4.2 alternatively w.r.t. C and T. It starts from $T_0 = \mathbf{I}d$ at iteration 0 (after a possible rigid or affine initialization); then, at iteration n, the alternated minimization scheme gives the following steps.

- Find C_n by minimizing $S(I,J,C_n) + \sigma||C_n - T_{n-1}||^2$. This is done in PASHA using gradient descent.
- Find T_n by minimizing $||C_n - T_n||^2 + \lambda R(T_n)$. This minimization step has a closed-form solution, using convolution.

Chapter 5

Displacements field, computation and analysis

5.1 Introduction

In order to propose a biomechanical model of the brain that would be as realistic as possible, we need to extract typical boundary conditions as well as an average brain constitutive mechanical law from experimental data (pre and post operative Parkinsonians MRI). These characteristic features are difficult to obtain by just looking at the images. We propose in this chapter to extract these characteristic features from the displacement field (computed by the non-rigid registration of pre to post operative brain, segmented in previous chapter) and its derivative (deformation tensor) analysis. This analysis allows us to extract more relevant information about the deformation.

5.2 Registration of pre and post operative MRI : Displacement field analysis

5.2.1 Displacement field analysis

In order to analyze the deformations that occurs in the brain, we have computed the non rigid displacement field between the two pre and post-operative MRI from 7 cases of Parkinsonians. We have used the PASHA algorithm (Chapter 3.2) to compute the displacement fields. Previous work of Alexis Roche at Al. ([24]) have demonstrated the importance of choosing a similarity criterion adapted to joint histograms. In our case, both images are obtained with the same acquisition modality (a T1 weighted MRI scan), so that the relation between our two images is close to identity. Therefore we have used a simple sum of squared intensity differences as a similarity criterion. To optimize the registration process, we have performed the algorithm in two steps :

- The first one consists in a rigid registration, performed with the ALADIN software (more information about ALADIN can be found in Sébastien Ourselin's theses [8]).
- The second one is a non-rigid registration, computed with the PASHA software, initialized with the rigid transformation.

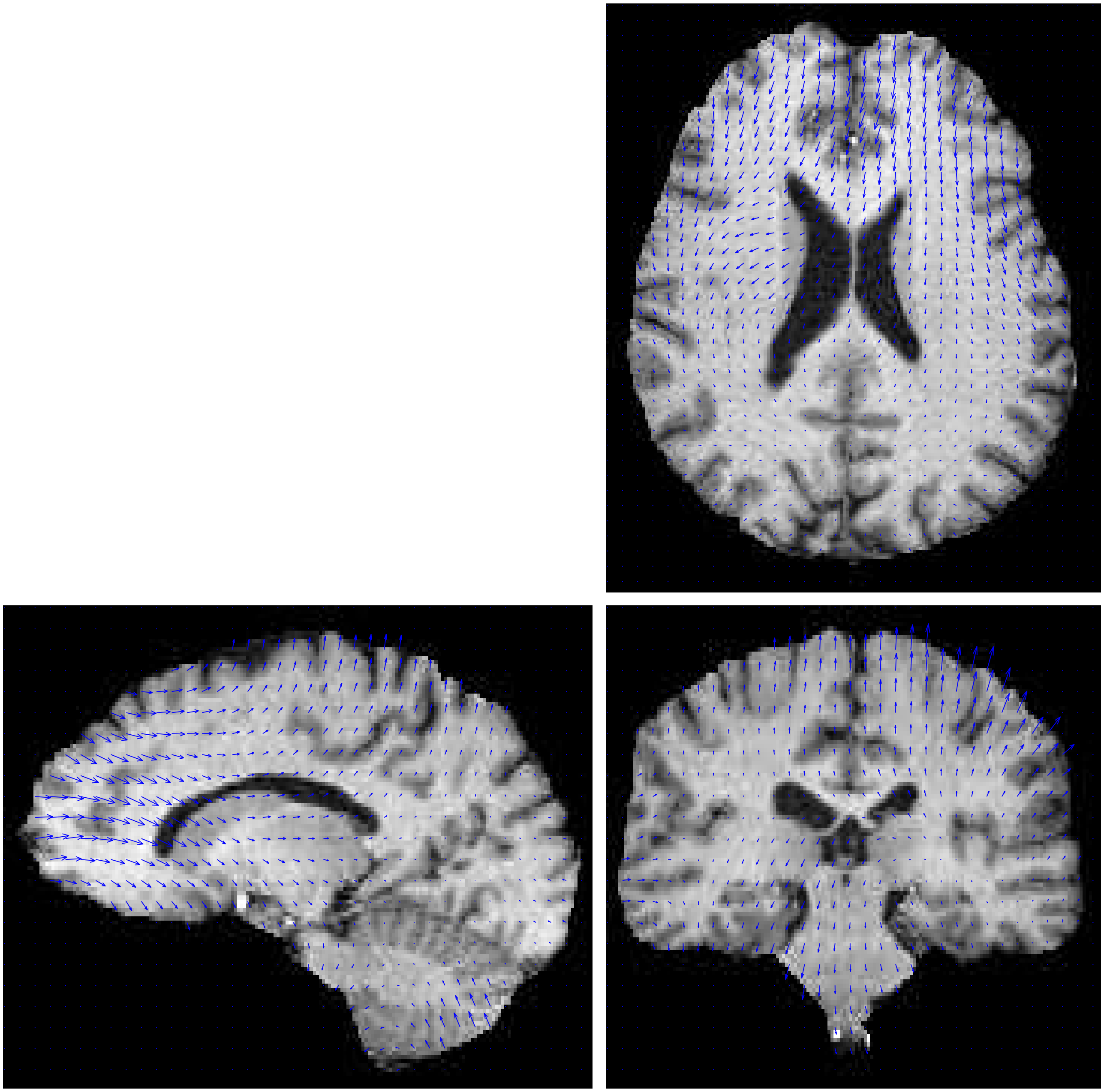

Figure 5.1: Displacement field for the patient's largest brain shift (case 6)

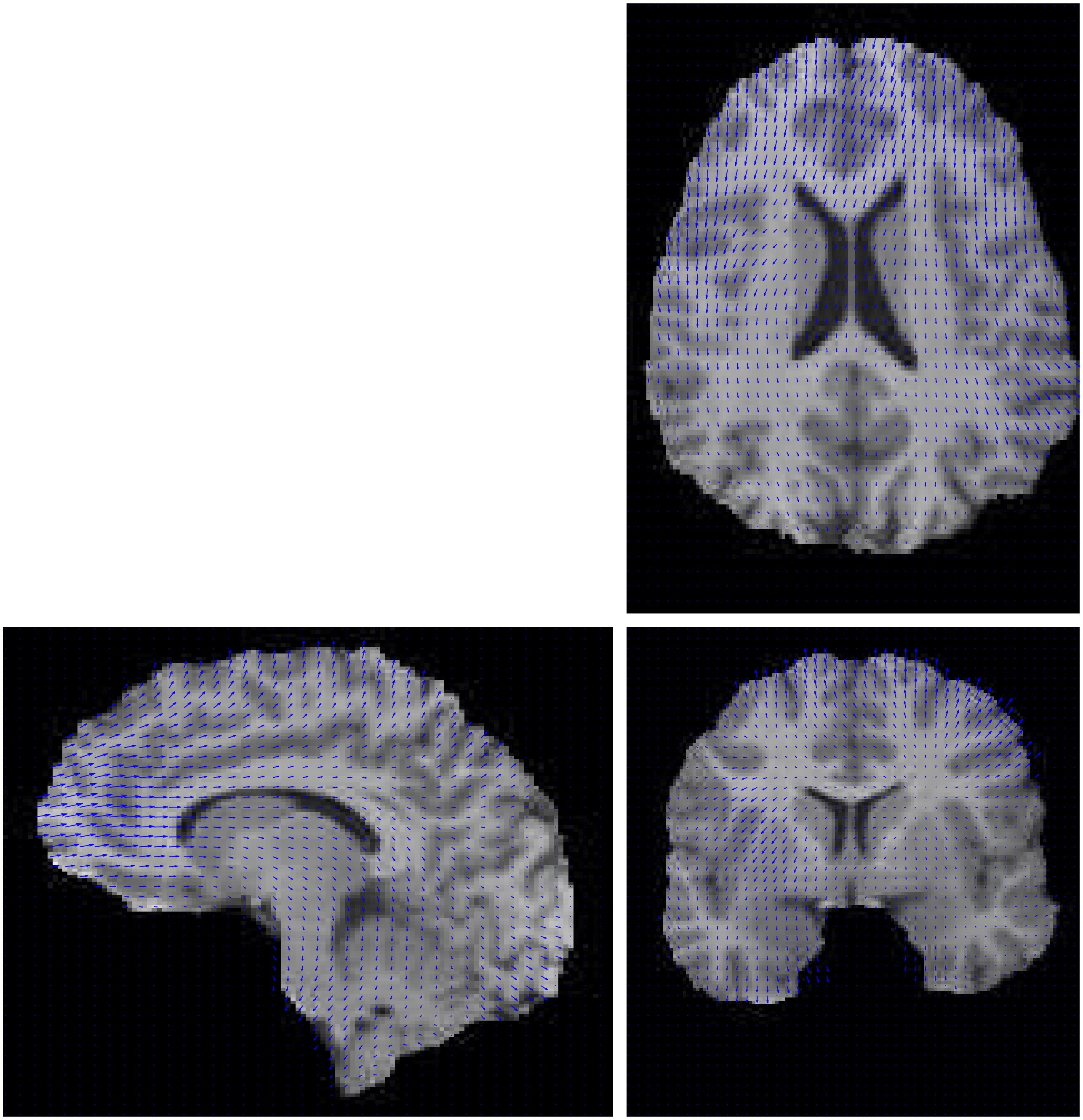

Figure 5.2: Average displacement field over the 7 cases, affine registered on the atlas brain.

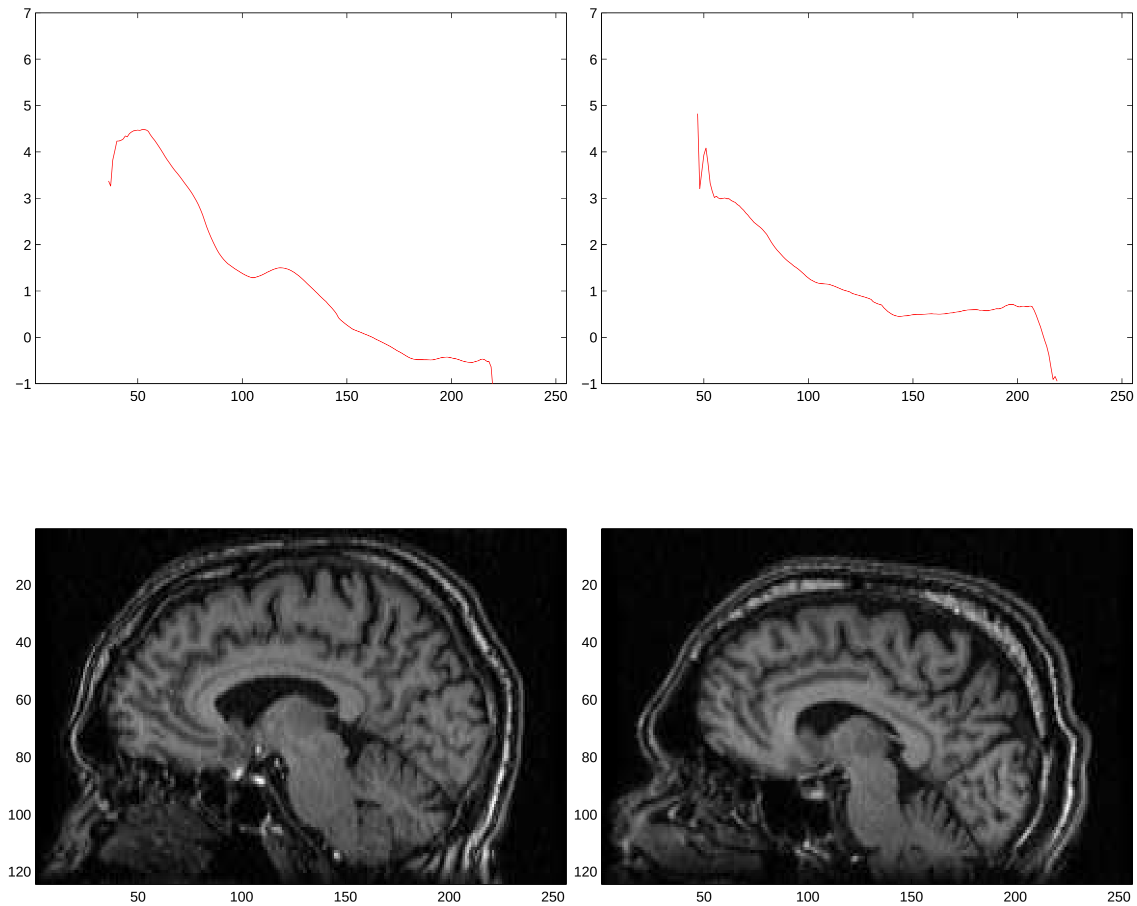

Figure 5.3: Average displacement of the axial cross sections along the gravity direction.

Figure 5.1 represents the displacement field obtained for three cuts of the largest brain shift image in the database. Figure 5.2 represents the average displacement field over the 7 cases, registered on the atlas MRI. One can, from these first images, put forward different phenomena :

- The assumption that displacement direction is aligned the gravity one made in the different papers quoted in chapter 1.3 is confirmed. The average displacement direction of the brain structures makes an angle of 17 degrees with the gravity direction.
- The procedure introduces very important artifacts on both the post operative MRI and the displacement field computed by the non-rigid algorithm. These artifacts are of different nature :
  - The existence of instruments (the electrode) in the second MR Image.
  - The metallic nature of the electrode, spreads high intensity voxels around the electrodes, reinforcing the previous observation.
  - A third one is due to tissue opening which cannot be modelled by a regular displacement field.
- We have observed for almost each case an important asymmetry in the displacement field of the two

hemispheres. However this asymmetry is already directly distinguishable on the pre end post operative MRI (see Figure 3.2 to be convinced.)

In addition to the displacement field, we have also computed the average displacement of axial cross sections in the gravity direction. Figure 5.3 show this displacement for the two patients with the largest brain shift (cases 6 and 7). We have observed a significant variability in the results, depending on the weight of the regularization term in the PASHA algorithm as well as the method used to avoid artifacts influence : indeed the regularization parameter tend to balance the displacement field at the frontier of the brain. Depending on its intensity, the artefact sometimes really disturbs the displacement field around the subthalamic nucleus (the target of the electrodes). We must then consider very carefully these plots. Nevertheless, we can extract some general information about them :

- If we trust the rigid registration, we observe that the base of the brain (ie. the lowest part in the gravity direction) almost never moves (every case have a displacement < 1 mm).
- The frontal lobe seems to deform in a larger proportion relatively to the rest of the brain.
- We have noticed on most of the 7 cases (the one having the largest deformations) a local displacement equivalent to a rigid motion in the corpus callosum area. We propose two areas of investigation to find an anatomical explanation of this phenomenon :
  - The corpus callosum is mechanically fixed between the falx cerebri and the skull (see figure 8.3 in the *anatomy reminder* part for more details). It may only have a very limited margin of displacement. More specifically, the corpus callosum would collide with the Falx in its lowest part and would prevent this area of the brain to move.
  - The brain deformation is maximum in this area so that the brain may touch the parietal bone. Because of its incompressibility behaviour, as long as the brain is in contact with the skull, it can only slide along it with a local rigid motion comportment.

5.2.2 Deformation tensor analysis

To analyze displacement fields obtained from the non rigid software, we have tried out different continuum mechanics operators to synthesize the relevant information. From this point of the document, we will note the vector gradient as following :

$$\nabla \overrightarrow{f} = \begin{pmatrix} \frac{\partial f_x}{\partial x} & \frac{\partial f_x}{\partial y} & \frac{\partial f_x}{\partial z} \\ \frac{\partial f_y}{\partial y} & \frac{\partial f_y}{\partial y} & \frac{\partial f_y}{\partial z} \\ \frac{\partial f_z}{\partial z} & \frac{\partial f_z}{\partial z} & \frac{\partial f_z}{\partial z} \end{pmatrix}$$

Φ denote the relation which associates the new position vector of a material point $\underline{X}$ from its rest position after transformation in a fixed reference (see figure 5.4).

$$\Phi(\mathbf{X}) = \mathbf{X} + \mathbf{U}(\mathbf{X}). \tag{5.1}$$

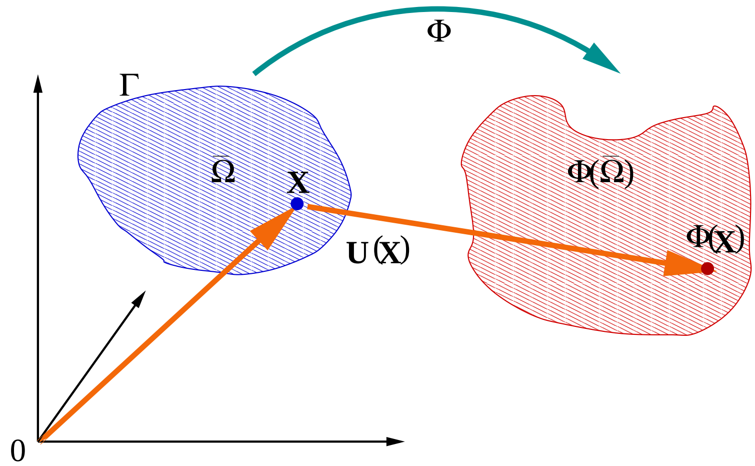

Figure 5.4: Deformation applied on a domain of $\mathbb{R}^3$

The displacement function $\mathbf{U}(\mathbf{X})$ is defined as :

$$\mathbf{U}(\mathbf{X}) = \Phi(\mathbf{X}) - \mathbf{X}$$

And the transformation gradient $\mathbf{F}$ at point $\mathbf{X}$:

$$\mathbf{F} = \nabla\Phi(\mathbf{X}) = \nabla\mathbf{U}(\mathbf{X}) + \mathbf{1}$$

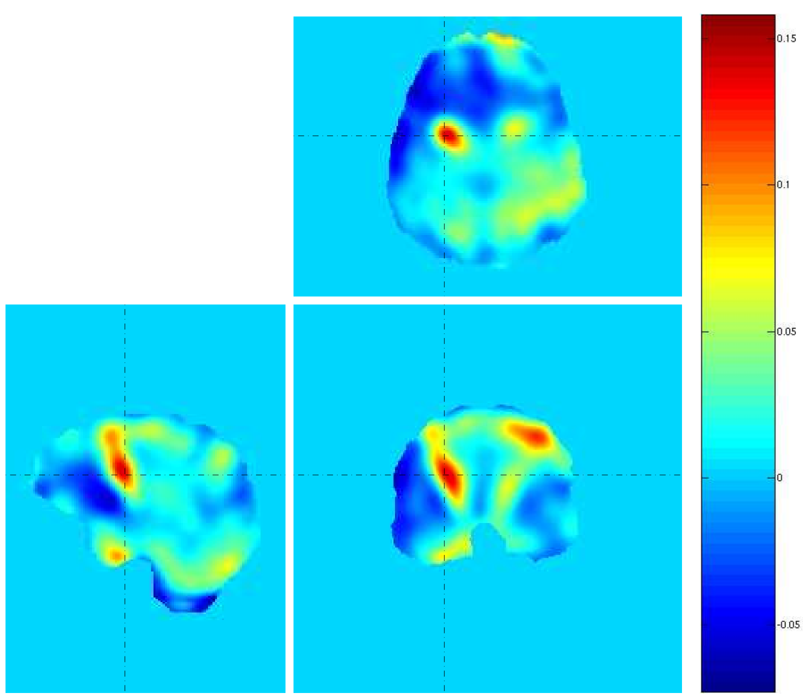

Figure 5.5: Local deformation rate : $\frac{d\Omega - d\Omega_0}{d\Omega_0}$.

We can then compute the local volumetric rate of deformation defined as the ratio of the local volume variation by the initial volume :

$$d\Omega = \det[\delta x', \delta y', \delta z'] = \det[\nabla\Phi \cdot \delta x, \nabla\Phi \cdot \delta y, \nabla\Phi \cdot \delta z] = \det[\nabla\Phi] \cdot \det[\delta x, \delta y, \delta z] = \det[\nabla\Phi] d\Omega_0$$

$$\frac{d\Omega}{d\Omega_0} = \det[\nabla\Phi] = det(\mathbf{F})$$

$$\frac{d\Omega - d\Omega_0}{d\Omega_0} = det(\mathbf{F}) - \mathbf{1} \tag{5.2}$$

Figure 5.5 presents the local deformation rate computed from the observed displacement field. We can make new assumptions based on this image :

- The material is globally incompressible, with a compression rate comprised between +5% and -5%.
- Large compression rate values (over 15%) are logically produced around electrode artifacts.

The Green-Lagrange deformation tensor **E** is then given by :

$$\mathbf{E} = \frac{1}{2}\left(\nabla\mathbf{U}^t + \nabla\mathbf{U} + \nabla\mathbf{U}^t\nabla\mathbf{U}\right) \tag{5.3}$$

And the linearized version of the Green Lagrange tensor :

$$\mathbf{E}_{lin} = \frac{1}{2}\left(\nabla\mathbf{U}^t + \nabla\mathbf{U}\right) \tag{5.4}$$

Explicitly, the matrix **E** is :

$$\mathbf{E} = \frac{1}{2}\begin{bmatrix} 2\,\varepsilon_x & \gamma_{xy} & \gamma_{xz} \\ \gamma_{xy} & 2\,\varepsilon_y & \gamma_{yz} \\ \gamma_{xz} & \gamma_{yz} & 2\,\varepsilon_z \end{bmatrix} \text{ où } \begin{cases} \varepsilon_x = u_x + \frac{1}{2}(u_x^2 + v_x^2 + w_x^2) \\ \varepsilon_y = v_y + \frac{1}{2}(u_y^2 + v_y^2 + w_y^2) \\ \varepsilon_z = w_z + \frac{1}{2}(u_z^2 + v_z^2 + w_z^2) \\ \gamma_{xy} = (u_y + v_x) + (u_x u_y + v_x v_y + w_x w_y) \\ \gamma_{xz} = (u_z + w_x) + (u_x u_z + v_x v_z + w_x w_z) \\ \gamma_{yz} = (v_z + w_y) + (u_y u_z + v_y v_z + w_y w_z) \end{cases} \tag{5.5}$$

One can have a physical representation of each term in the Green-Lagrange deformation tensor (see figure 5.6): diagonal terms represent the stretching deformation and extra-diagonal terms represent the shearing deformation.

The eigenvector corresponding to the largest eigenvalue of the Green Lagrange tensor represents the main direction of deformation. This direction physically represents the main strain direction in the brain material. Figures 5.7 shows this eigenvectors, weighted with their eigenvalues for the largest brain shift MRI, placed on the post operative MRI.

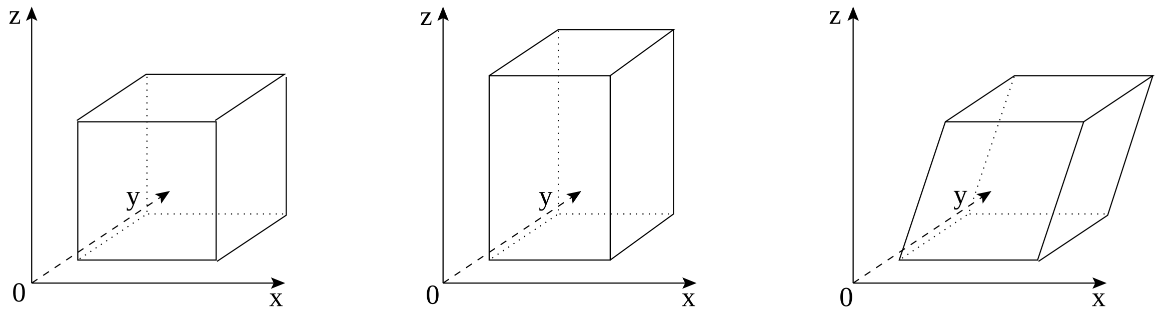

(a) Rest position (b) $\varepsilon_z \neq 0$ (c) $\gamma_{xz} \neq 0$

Figure 5.6: Physical representation of the Green-Lagrange deformation tensor **E** terms.

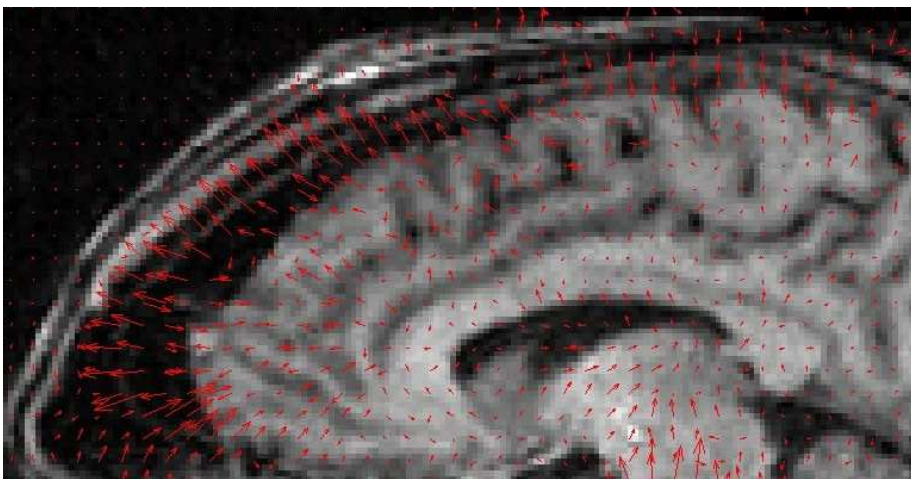

Figure 5.7: Zoom on the main strain direction computed (for patient 6).

Whereas this last analysis show the evidence of main strain direction orthogonal to the contact surface cortex / dura mater, we need to go in further investigation about this result. Actually, because of the regularization of the displacement field, especially at the brain frontier where the real displacement field gradient is very high and oriented along the surface normal, it is difficult to distinguish the regularization effect from mechanical real deformation.

Chapter 6

Finite element modeling of elastic material

6.1 Introduction

The building of a physically-based deformable model must follow different steps. After generating the tetrahedral mesh, we have to choose a biomechanical constitutive law of the material, based on continuous mechanics laws. Although brain tissues are neither isotropic nor linear, we have used for this first model linear isotropic laws. The next step is boundary conditions determination, depending on the observed behaviour. Last step is the computation of the solution. This chapter is dedicated to the continuum mechanics : elasticity laws, rigidity force and displacement matrix, boundary conditions and problem resolution.

6.2 Elastic laws

6.2.1 hyper-elastic materials

A material is said **elastic** when its stress tensor uniquely depends on the position and on deformation gradient. Furthermore this material is said **hyper-elastic** if there exists a potential energy function W such as the Cauchy stress tensor can be written :

$$\Sigma = \nabla\Phi^{-1}\, T = \frac{\partial W}{\partial E}. \tag{6.1}$$

Global energy for an entire domain Ω is then computed from this potential energy with :

$$\mathcal{E} = \int_{\Omega} W \, d\mathbf{X} \tag{6.2}$$

With defining the deformation tensor $\mathbf{C}$:

$$\mathbf{C} = \nabla\Phi^t \, \nabla\Phi. \tag{6.3}$$

The energy function W for an homogeneous and isotropic material is computed from the roots of the polynomial $det(C - \lambda I)$ and can be written from the tensor $\mathbf{C}$ or tensor $\mathbf{E}$:

$$\begin{cases} l_1 = & trC & = 3 + 2trE \\ l_2 = & \frac{1}{2}\left((trC)^2 - trC^2\right) & = 3 + 4trE + 2\left[(trE)^2 - trE^2\right] \\ l_3 = & |C| & = |2E + I| \end{cases} \tag{6.4}$$

The energy function for an hyper-elastic material is then

$$W = \sum_{r,s,t=0}^{\infty} L_{rst}(l_1-3)^r(l_2-3)^s(l_3-1)^t, \quad L_{000}=0 \tag{6.5}$$

6.2.2 St Venant-Kirchhoff elastic model

St Venant-Kirchhoff elastic model is defined from equation 6.5 with every L_{rst} null except :

$$L_{100}=\mu, \quad L_{200}=\frac{\lambda+2\mu}{8} \quad \text{et} \quad L_{010}=-\frac{\mu}{2} \tag{6.6}$$

Potential elastic energy of a St Venant-Kirchhoff material is then defined with :

$$W=\frac{\lambda}{2}(trE)^2+\mu\, trE^2, \tag{6.7}$$

λ and μ are the *Lamé* constants. They are related to the classical material properties **Young modulus** E and **Poisson ratio** with :

$$\lambda=\frac{E\nu}{(1+\nu)(1-2\nu)} \qquad \mu=\frac{E}{2(1+\nu)} \tag{6.8}$$

6.3 Potential elastic energy : *Hooke*'s law

Linear elasticity is part of the St Venant-Kirchhoff model. With linearizing the **E** tensor in equation 5.4, W^l energy can be computed from the displacement field by :

$$W^l=\frac{\lambda}{2}(div\,\mathbf{U})^2+\mu\|\nabla\mathbf{U}\|^2-\frac{\mu}{2}\|rot\,\mathbf{U}\|^2 \tag{6.9}$$

where **f** is the external force applied on the domain. Except in very simple cases, this equation solution cannot be computed directly. That is why we need to discretise the problem to compute a numerical solution. Therefore we will use the finite element method.

6.4 Linear elasticity in Finite Element Modeling

The FEM consists in dividing the considered domain into sub-domain in which material behaviour is entirely defined. In our case, we use linear interpolation with tetrahedral element P1.

The first step is to write the displacement function into the element and compute its gradient :

$$\boxed{\mathbf{U}(\mathbf{X}) = \sum_{j=0}^{3} \Lambda_j(\mathbf{X})\ \mathbf{U}_j} \tag{6.10}$$

$$\text{où} \quad \begin{cases} \Lambda_j(\mathbf{X}) = \alpha_j \,.\, \mathbf{X} + \beta_j,\ j = 0..3, \\ \text{are linear interpolation functions, and} \\ \\ \mathbf{U}_j = \mathbf{U}(\mathbf{P}_j),\ j = 0..3, \\ \text{are vertex displacements.} \end{cases}$$

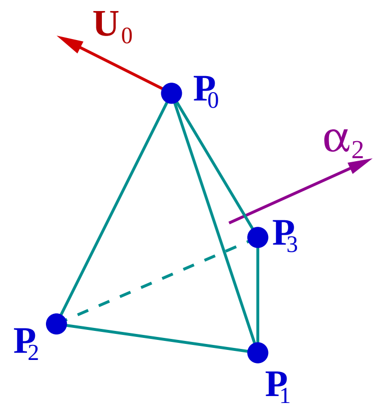

FIG. 6.1 – *Finite element of type* P_1 *(linear interpolation)*

We can then express the gradient function in the tetrahedral volume :

$$\nabla\mathbf{U} = \sum_{j=0}^{3} \mathbf{U}_j\ \nabla\left(\alpha_j \,.\, \mathbf{X} + \beta_j\right) = \sum_{j=0}^{3} \mathbf{U}_j\ \alpha_j^t$$

$$\Longrightarrow \boxed{\nabla\mathbf{U} = \sum_{j=0}^{3} \mathbf{U}_j \otimes \alpha_j} \tag{6.11}$$

This strain is constant inside each tetrahedron, so will be piecewise constant on the entire mesh. We can then compute the associated energy in the tetrahedron in equation 6.9 :

$$\boxed{W^l(\mathcal{T}) = \frac{1}{2} \sum_{j,k=0}^{3} \mathbf{U}_j^t \left[\mathcal{B}_{\mathcal{T}}^{jk}\right] \mathbf{U}_k \quad \text{avec} \quad \mathcal{B}_{\mathcal{T}}^{jk} = \lambda\left(\alpha_j \otimes \alpha_k\right) + \mu\Big[(\alpha_k \otimes \alpha_j) + (\alpha_j \,.\, \alpha_k)\, Id\Big]} \tag{6.12}$$

matrices $\left\{\mathcal{B}_{\mathcal{T}}^{jk}\ ;\ j,k = 0..3\right\}$ represent the elementary rigidity tensor of tetrahedron $\mathcal{T}$ linking the displacement vector $\mathbf{U}$ to the force vector $\mathbf{F}$. One can easily demonstrate that $[\mathcal{B}_{\mathcal{T}}^{kj}] = [\mathcal{B}_{\mathcal{T}}^{jk}]^t$. Therefore 10 tensors per tetrahedra only are necessary to describe the strain/stress relation. These tensors can also be seen as the local rigidity tensor associated to vertex and edges.

$$\mathbf{F}_p^l(\mathcal{T}) = \sum_{j=0}^{3} \left[\mathcal{B}_{\mathcal{T}}^{pj}\right] \mathbf{U}_j$$

$$\Longleftrightarrow \boxed{\mathbf{F}_p^l(\mathcal{T}) = \left[\mathcal{B}_{\mathcal{T}}^{pp}\right] \mathbf{U}_p + \sum_{\substack{j=0 \\ j \neq p}}^{3} \left[\mathcal{B}_{\mathcal{T}}^{pj}\right] \mathbf{U}_j} \tag{6.13}$$

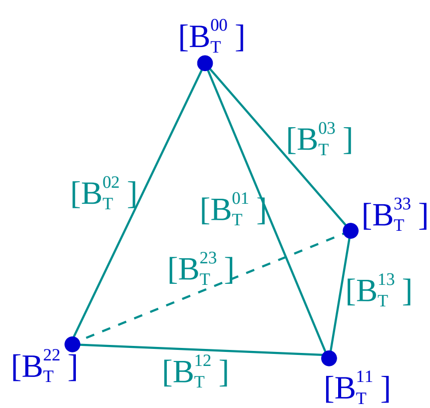

FIG. 6.2 – *Decomposition of the elementary rigidity matrix on vertices and edges.*

6.5 Solving the FEM problem

6.5.1 Assembling the total rigidity matrix

The global rigidity matrix **K** is then assembled from the elementary rigidity matrices $\mathcal{B}^{pp}$ and $\mathcal{B}^{pj}$. The size of this matrix is ($3N_s$ x $3N_s$) with N_s the number of vertices in the mesh. The static mechanical problem can then be written as $[K]\,\mathbf{U} = \mathbf{F}$:

$$\begin{bmatrix} \mathcal{B}^{0,0} & \dots & \mathcal{B}^{0,p} & \dots & \mathcal{B}^{0,N_s-1} \\ \vdots & \ddots & \vdots & & \vdots \\ \mathcal{B}^{p,0} & \dots & \mathcal{B}^{p,p} & \dots & \mathcal{B}^{p,N_s-1} \\ \vdots & & \vdots & \ddots & \vdots \\ \mathcal{B}^{N_s-1,0} & \dots & \mathcal{B}^{N_s-1,p} & \dots & \mathcal{B}^{N_s-1,N_s-1} \end{bmatrix} \begin{bmatrix} \mathbf{U}_0 \\ \vdots \\ \mathbf{U}_p \\ \vdots \\ \mathbf{U}_{N_s-1} \end{bmatrix} = \begin{bmatrix} \mathbf{F}_0 \\ \vdots \\ \mathbf{F}_p \\ \vdots \\ \mathbf{F}_{N_s-1} \end{bmatrix} \tag{6.14}$$

Because the local rigidity matrix $\mathcal{B}^{pj}$ is not null only if vertices$\mathbf{P}_p$ and $\mathbf{P}_j$ have a common edge, the matrix K is sparse.

6.5.2 Applying boundary conditions

Applying boundary condition amounts to modify the linear system 6.14. The easiest condition to apply is a force constrain $\mathbf{F}^*_p$ on a vertex. One only have to modify the **F** force vector :

$$\begin{bmatrix} \mathcal{B}^{0,0} & \dots & \mathcal{B}^{0,p} & \dots & \mathcal{B}^{0,N_s-1} \\ \vdots & \ddots & \vdots & & \vdots \\ \mathcal{B}^{p,0} & \dots & \mathcal{B}^{p,p} & \dots & \mathcal{B}^{i,N_s-1} \\ \vdots & & \vdots & \ddots & \vdots \\ \mathcal{B}^{N_s-1,0} & \dots & \mathcal{B}^{N_s-1,p} & \dots & \mathcal{B}^{N_s-1,N_s-1} \end{bmatrix} \begin{bmatrix} \mathbf{U}_0 \\ \vdots \\ \mathbf{U}_p \\ \vdots \\ \mathbf{U}_{N_s-1} \end{bmatrix} = \begin{bmatrix} \mathbf{F}_0 \\ \vdots \\ \boxed{\mathbf{F}^*_p} \\ \vdots \\ \mathbf{F}_{N_s-1} \end{bmatrix} \tag{6.15}$$

To apply a position constrain $\mathbf{U}^*_p$, one have to modify the rigidity matrix as well as the force constrain to remove the vertex contribution on each of its adjacent vertex :

$$\begin{bmatrix} \mathcal{B}^{0,0} & \dots & \begin{smallmatrix} 0&0&0\\0&0&0\\0&0&0 \end{smallmatrix} & \dots & \mathcal{B}^{0,N_s-1} \\ \vdots & \ddots & \vdots & & \vdots \\ \begin{smallmatrix} 0&0&0\\0&0&0\\0&0&0 \end{smallmatrix} & \dots & \begin{smallmatrix} 1&0&0\\0&1&0\\0&0&1 \end{smallmatrix} & \dots & \begin{smallmatrix} 0&0&0\\0&0&0\\0&0&0 \end{smallmatrix} \\ \vdots & & \vdots & \ddots & \vdots \\ \mathcal{B}^{N_s-1,0} & \dots & \begin{smallmatrix} 0&0&0\\0&0&0\\0&0&0 \end{smallmatrix} & \dots & \mathcal{B}^{N_s-1,N_s-1} \end{bmatrix} \begin{bmatrix} \mathbf{U}_0 \\ \vdots \\ \mathbf{U}_p \\ \vdots \\ \mathbf{U}_{N_s-1} \end{bmatrix} = \begin{bmatrix} \mathbf{F}_0 \boxed{-\mathcal{B}^{0,p}\,\mathbf{U}^*_p} \\ \vdots \\ \boxed{\mathbf{U}^*_p} \\ \vdots \\ \mathbf{F}_{N_s-1} \boxed{-\mathcal{B}^{N_s-1,p}\,\mathbf{U}^*_p} \end{bmatrix} \tag{6.16}$$

6.5.3 Solving the problem

The last step is the problem resolution. Once boundary condition have been applied, we have to solve the system :

$$[K]\,\mathbf{U} = \mathbf{F}$$

In reality,stiffness matrix inverse $[K]^{-1}$ is not explicitly computed. Due to the sparseness of $[K]$, we precondition matrix $[K]$ with incomplete cholesky method (similar to a LU decomposition) using tools of the Matrix Template Library (see http://www.osl.iu.edu/research/mtl/ for more information). The final solution is obtained with the conjugate gradient method of the Iterative Template Library (see http://www.osl.iu.edu/research/itl/ for more information) taking as parameters the maximum number of iterations or/and a maximum residue.

Chapter 7

The biomechanical model and results

7.1 The biomechanical model

This part is dedicated to the construction of the patient-based biomechanical model. This part uses all the previous material presented in this report. We apply elasticity laws detailed in chapter 5.2.2 on the patient specific mesh presented in chapter 2.3.2. We then define boundary conditions based on the brain deformation analysis obtained in chapter 4.2. Finally, after computing the gravity induced deformation, we propose to quantify the prediction deformation with the non-rigid registration algorithm described in chapter 3.2

7.1.1 Material parameters

We propose a model for brain tissue's material which takes into account the observation made on the deformation :

❶ According to the deformation analysis made in chapter 5.2.2, we propose a brain tissue material almost incompressible. We have fixed its Poisson ratio to 0.45.

❷ With no a-priori information about the brain tissue stiffness, we have used the Young Modulus measured in Karol Miller experiments (See [16] for more details) $E = 2000Pa$. Equation 6.8 allows to obtain the Lamé constants :

$$\mu = 689 \ \lambda = 6200$$

❸ Without any information about the material anisotropy, we have assumed an isotropic material in this first model, with linear elasticity law.

7.1.2 Boundary conditions

With respect to the displacement field obtained in chapter 5.2.1, we propose a new model including the anatomy of the brain and the mechanics of static fluid.

❶ We consider that Cerebro Spinal Fluid leak leads to an equivalent liquid level in the skull. Then the brain part under this liquid level is subject to different forces : The fluid force applied on the brain surface and the gravity :

- The local volumic force induced by gravity is :

$$\mathbf{F}_{Gravity} = -\int_{Brain\ Volume} \rho.g.dV$$

- Considering no friction between the brain and the skull, fluid force applied on the brain is :

$$\mathbf{F}_{Fluid} = \iint_{Brain\ Surface} P_{fluid \to brain}.dS$$

Mechanics of static fluid gives the explicit pressure law in a fluid :

$$P_{fluid \to brain} = \rho.g.h + P_0$$

Combined with the Stokes equation :

$$\iint_{Brain\ Surface} P_{fluid \to brain}.dS = \iiint_{Brain\ Volume} grad(P).dV = \iiint_{Brain\ Volume} \rho.g.dV$$

- Therefore, if no friction exists between the brain and the skull, we can consider that the resultant force applied on the brain part under the liquid level is null.

❷ Brain part over the liquid level is subject to gravity only ($\int$ (air pressure) is balanced over the total surface of the emerged part). We have then applied on each tetrahedron's vertex the force :

$$\mathbf{F} = \Sigma_{Adjacent\ Tetrahedron}\left(-\iiint_{Tetrahedron\ Volume} \frac{\rho.g.dV}{4}\right)$$

❸ To take into account the asymmetry in the displacement field computed, we propose to separate the hydraulic behaviour of each hemisphere. This hypothesis is based on the anatomy (the falx cerebri) . But it is also based on the fact that during a Parkinson neuro-surgical procedure, the two hemispheres are treated one after the other. We have then a different CSF liquid level for each hemisphere leading to two different volumetric forces applied on each hemisphere.

❹ To balance the force moment due to the difference of forces between both sides, we have modelled the falx cerebri, allowing vertices belonging to tetrahedron intersecting the mid-sagital plane to slide along this plane.

❺ Finally, we have fixed vertices at the basis of occipital lob (on 15 % oh the total height) since figure 5.3 showed that the displacement at this part of the brain is close to zero.

All the boundary conditions are summarized in figure 7.1.

In order to find the best parameters for the model, we had to choose an error criterion to estimate the quality of the prediction. We have chosen to compute the sum of squared displacements over the brain obtained by registering the predicted MRI with the post-operative MRI :

$$Error = \iiint_{Brain\ Volume} \left|\overrightarrow{Displacement}\right|^2.dV$$

All of the following tests have been performed on case 6, the largest brain shift patient.

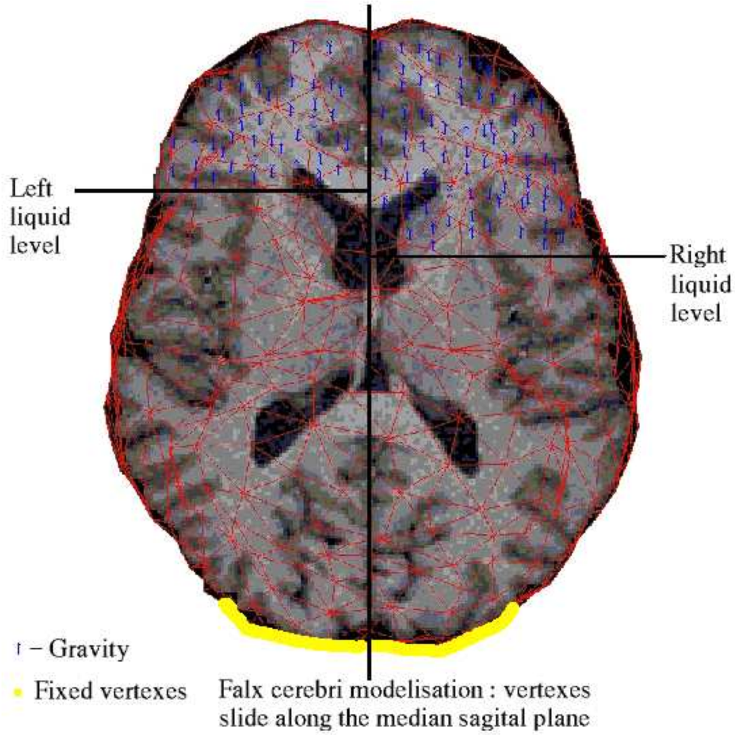

Figure 7.1: Boundary conditions applied to the biomechanical model.

7.2 Results

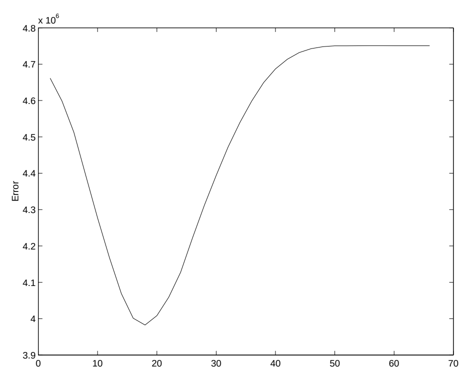

Figure 7.2: Prediction error as a function of the average CSF liquid level (% of the brain height)

First we tested if there exists an average CSF liquid level which explains the deformation. Figure 7.2 shows the evolution of the error criterion between the prediction and the post-operative MRI.

It allows us to estimate an average liquid level in the brain. This average liquid level, located at 18.5 % of the total height of the brain, minimizes the computed error with the post-operative MRI.

However, this average liquid level cannot recover the asymmetry observed in most case displacement field. So we then have tried out the asymmetrical model, with two different liquid levels for each hemisphere. Figure

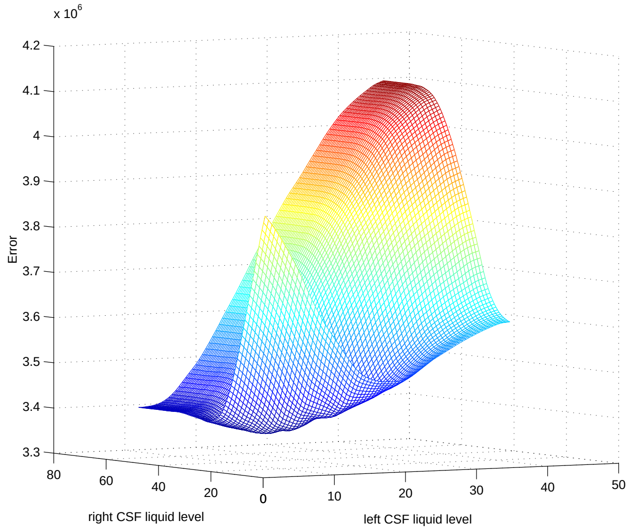

Figure 7.3: Prediction error depending on the average CSF liquid level (% of the brain height) in each hemisphere

7.3 shows the evolution of the error criterion as a function of left and right CSF liquid levels.

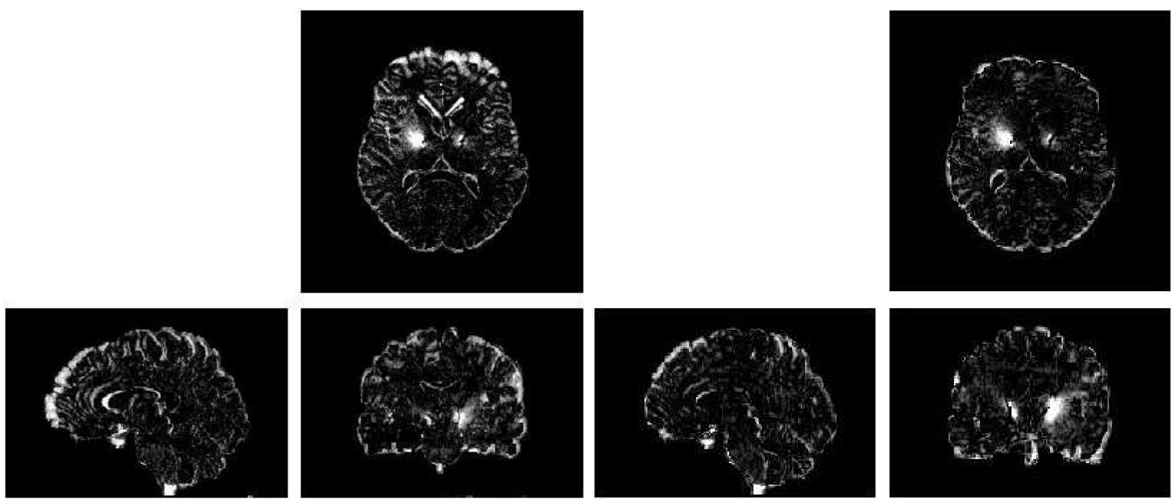

Difference pre / post-operative MRI   Difference predicted / post-operative MRI.

Figure 7.4: Comparison of difference images with and without prediction.

One can notice that the error criterion converges to a minimum, which means that we can find two CSF liquid level for each hemisphere able to explain the asymmetrical deformation. The "valley" observed on the plotted graphic numerically correspond to an average of the two liquid levels equal to the previously computed one (ie $\frac{Level_1+Level_2}{2} \simeq 18,5\%$).

Figure 7.4 presents the absolute difference of pre and post-operative MRI compared to the absolute difference of predicted end post-operative MRI. The predicted MRI have been computed with the two parameters that minimize the global error on figure 7.3. We can verify that our model is able to balance the brain shift phenomenon as well as the asymmetry. Nevertheless, the model does not seem to reduce the difference residue on the sulcus area. This problem is, in our opinion, due to homogeneous material model proposed for the full brain and maybe also to displacement boundary conditions imposed at the base of the occipital lobe.

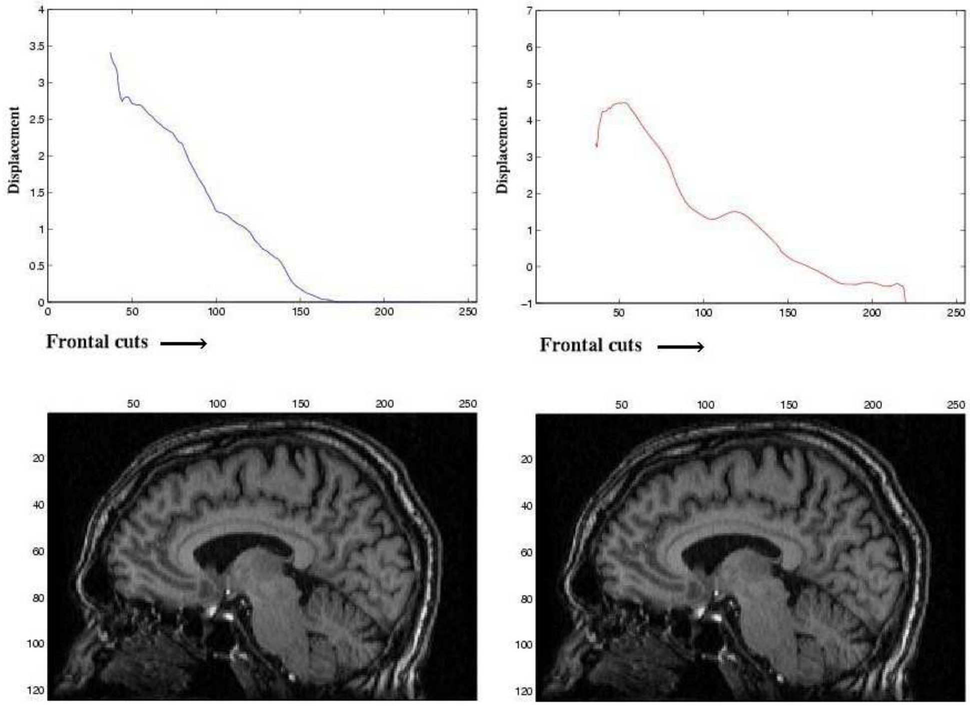

Figure 7.5: Average displacement of axial cross sections along the gravity direction for prediction (left) and real case (right)

The observation of the computed displacement field for frontal cuts along the gravity direction on figure 7.5 shows that the global displacement function is quite well transcribed.
However, we need to get into further investigation about specific part of the displacement function, and especially :

- identify regularization's influence in the registration process at the ends of the plotted graph.
- isolate the mechanical function of the corpus callosum area.

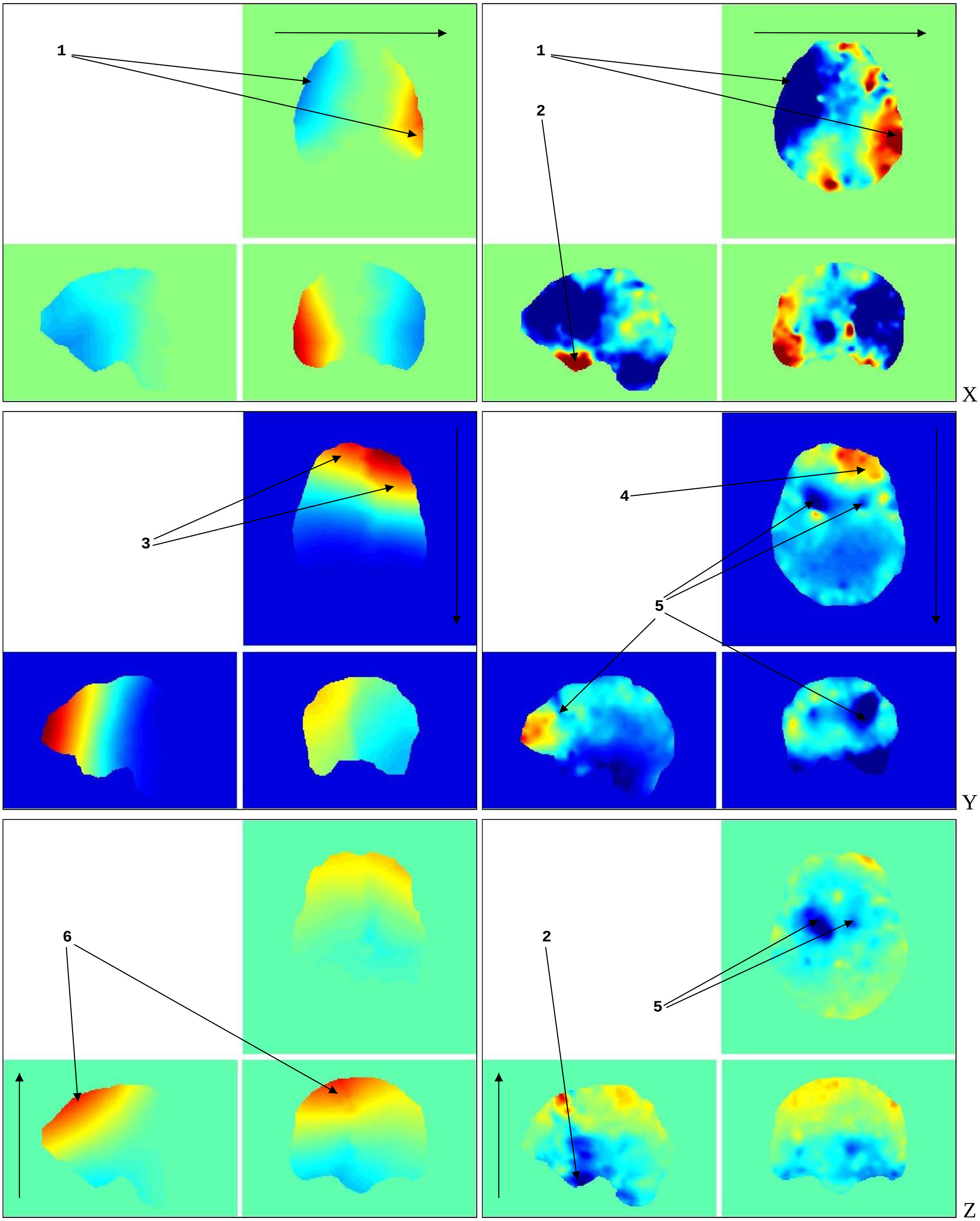

Figure 7.6: Displacement field predicted (left) and obtained from the registration of pre and post operative MRIs (same scale). Displacement direction is indicated by the arrow on the side of each figure.

The direct comparison between the predicted displacement field and the measured one (figure 7.6) allows us to measure the quality of the biomechanical prediction :

❶ The global displacement of sagittal cross sections in the X direction is well transcribed by the model. Both scale and distribution are similar for the model and the prediction.

❷ According to the measured displacement, the basis of the temporal lob seems to deform much more in reality than on the mechanical model. Nevertheless, we must be careful about this significant difference. It has no anatomical justification and might come from the registration algorithm.

❸ The model quantitatively well relates the asymmetry along the gravity direction.

❹ However, the measured asymmetry does not look as regular as the simulated one. We might consider a non linear comportment for the brain parenchyma to explain the differences between the two displacements.

❺ As previously seen in the displacement analysis chapter, the measured displacement is very disturbed in the electrode area. We thus have no way to estimate the accuracy of the displacement in this area.

❻ Finally, the predicted displacement in the Z direction of the frontal lob area is significantly higher than the measured one. We propose then to prevent the brain to move too far in the Z direction by adding the **contact with the skull** to the model.

Chapter 8

Conclusion and future work

8.1 Conclusion

In this report, we first presented an overview of existing biomechanical models of the human brain. As can be seen in the **State of the art** chapter, most of the biomechanical model proposed in the literature are used to interpolate displacements in the whole brain volume. They use intra-operative information to assign displacements boundary conditions to a finite element model. These models are used during the surgical procedure to update both pre-operative MRI and surgical planning. Our predictive model, at the contrary, uses **forces** boundary condition to model the gravity induced deformation. The main application of such a model is found in the update of the pre-operative surgical planning, providing the surgeon useful information to estimate tissues displacements.

In chapter 3, we presented two different methods for segmenting the brain in the pre and post-operative MRI. We have encountered a large variability in the displacement field with respect to PASHA regularization parameters. We want to insist on the importance of the non-rigid algorithm, the computation of the vector field remaining a key point in our study and certainly in any deformation analysis. Actually, the algorithm, described in chapter 4, is used for both cortex segmentation, displacement analysis, and error calculation. Therefore we spent time on understanding the way the algorithm works and the role of its parameters.

In chapter 5 we reported the different methods used to analyze the displacement field. Using continuum mechanics operators, we proposed different way to analysis displacements and deformations. Based on this analyse, we extracted features of the brain shift phenomenon observed in the case of a neurosurgical procedure on the Parkinson disease.

Chapter 6 is dedicated to the finite element method. We briefly described the linear elasticity laws governing the model before detailing the resolution process. In chapter 7, we detailed the biomechanical model. We proposed in the first part the different force and displacement boundary conditions applied on the model taking into account the anatomy and previous displacements analysis. In the second part, we present the results obtained with this simple model.

This first study on predicting the brain shift phenomenon has demonstrated the ability of a biomechanical model predict gravity-induced deformations of the brain. The proposed model is, currently, able to render the global displacement field as well as balancing the asymmetrical effects. However, it still has some approximations, especially in the Z direction. Actually, the displacement observation reveals that the brain collides the skull in the pre-motor area of the frontal lobe. We have also observed a general error increase from the center of the brain to its surface, which might originate from the incompressibility constraint. In fact, discussions with surgeons revealed the leading role of physiological parameters on the mechanical behaviour of the brain. Mannitol effects, for example, could explain the problems encountered onthe brain surface.

To sum up, we can say that using a physics-based modeling (extracted from each patient's anatomy) to predict the brain shift seems to be well suited to explain the real deformations measured on pre-operative and post-operative MRIs. Although the model can not predict the entire deformation yet, we are very optimistic about these encouraging preliminary results. We wish to get further in this anatomy-based model by including several other anatomical structures, detailed in the next section. Combining anatomical and physiological constraints is likely to be, in the future, a very promising way of research in biomechanical modeling and more specifically in brain comportment understanding.

8.2 Future work

We wish, for future work, include patient-specific physiological constraints, almost never taken into account in the different model reviewed in the State of the art chapter. We wish to obtain a general biomechanical model of the brain by combining anatomical and physiological constraints :

- Modeling the collision between the frontal lobe and the skull seems necessary to minimize the experienced prediction error in the frontal lob area.
- Use different Lamé coefficients for white matter, grey matter and ventricles to take into account the inhomogeneity of the brain.
- Include anisotropy and fibers orientation of brain tissues in the mechanical comportment of our finite element model.
- Add the physical role of the corpus callosum.
- Take into account the friction between brain and skull. This point should moreover lead us to reconsider the gravity model, based on the Archimede's pressure.

In addition to these anatomical constraints, we wish to introduce physiological constraints in the model :

- Blood pressure.
- CSF pressure.
- Osmotic pressure.
- Cerebral perfusion pressure.

The objectives of our future model model can be synthesized by the following figure :

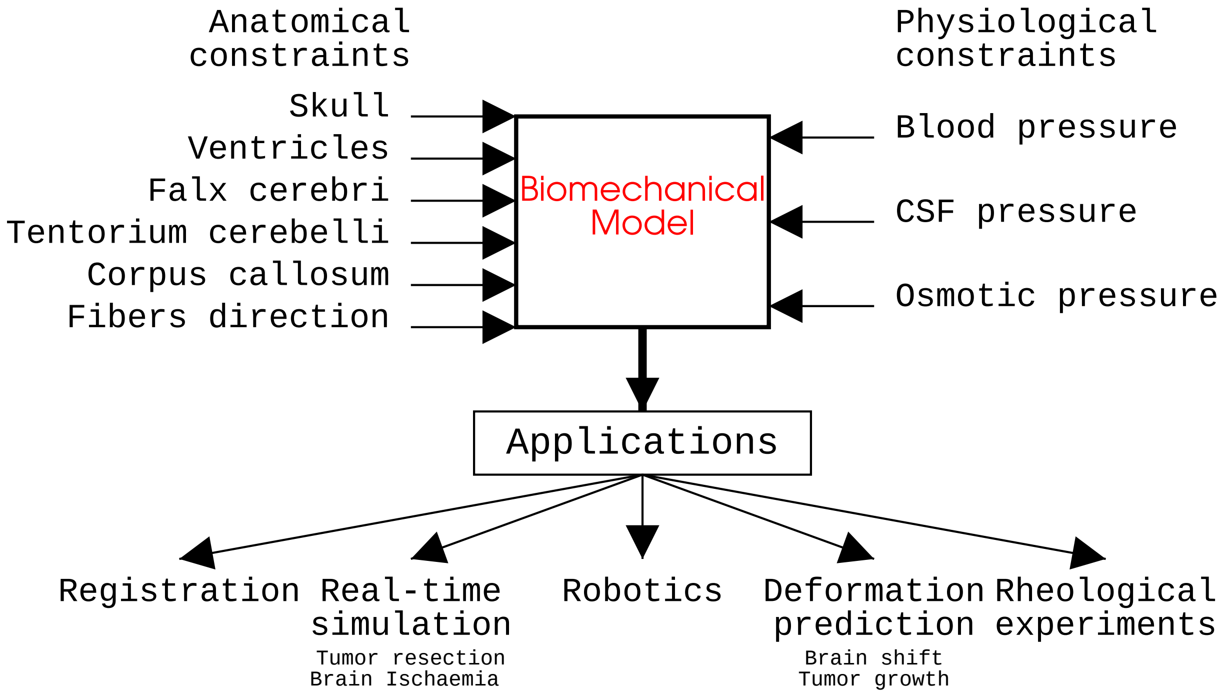

Such a biomechanical should allow us to explore new research tracks, including the current gravity induced deformation model. We are more specifically interested in modelling the effect of tumor resection on brain deformation and real-time surgery simulation. Combining these two areas of research would allow to predict the brain shift in many neurosurgical procedures. Such a model would be very useful to update the pre-operative planning depending on tumor localization as well as offering nice perspectives in surgical training.

Anatomy appendix

(All the following images originate from the digital anatomist project. http://www9.biostr.washington.edu/da.html)

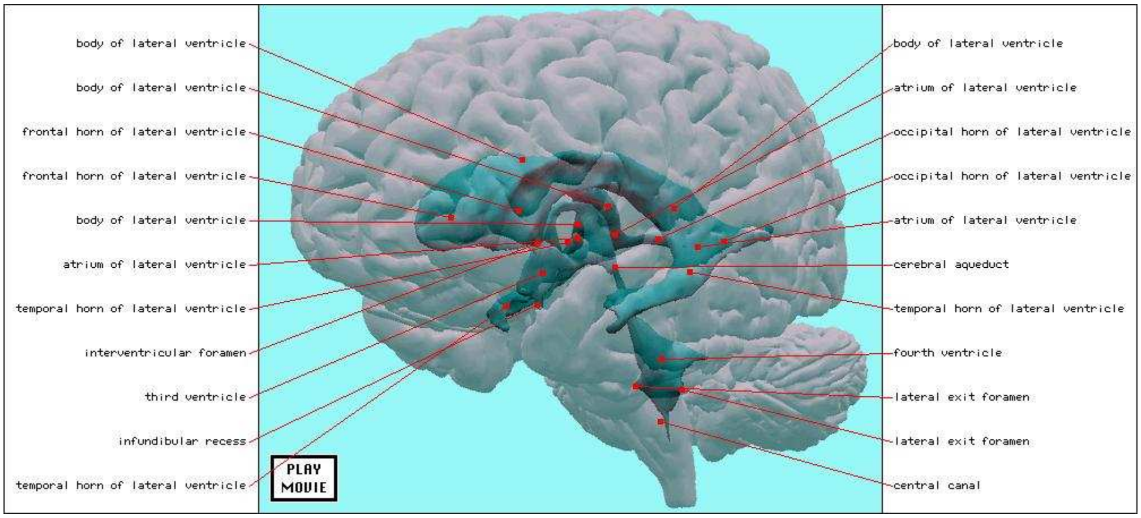

Figure 8.1: Ventricles and cortex.

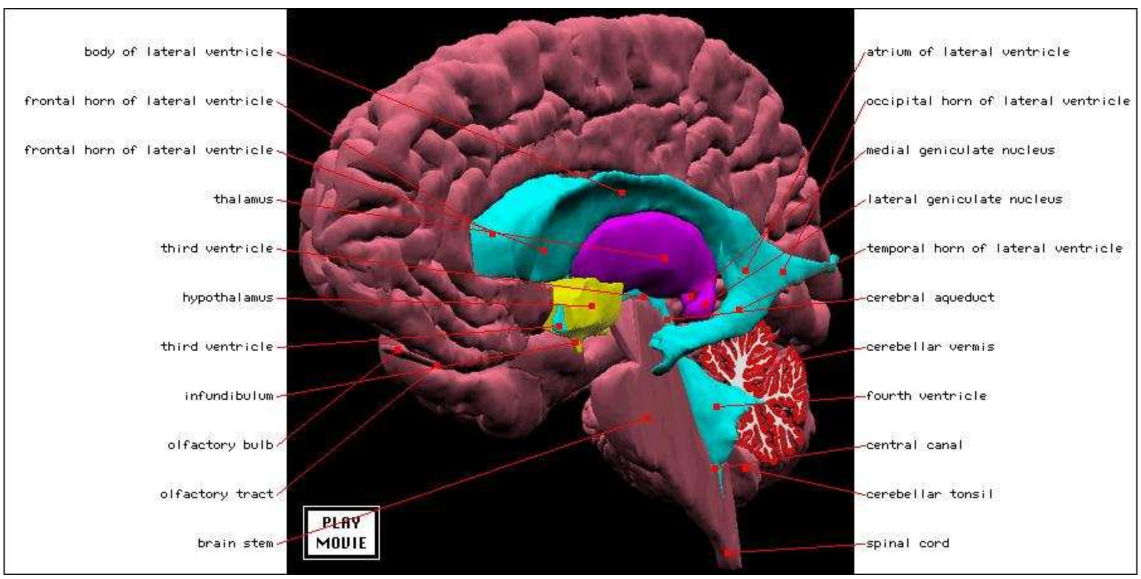

Figure 8.2: Thalamus and around

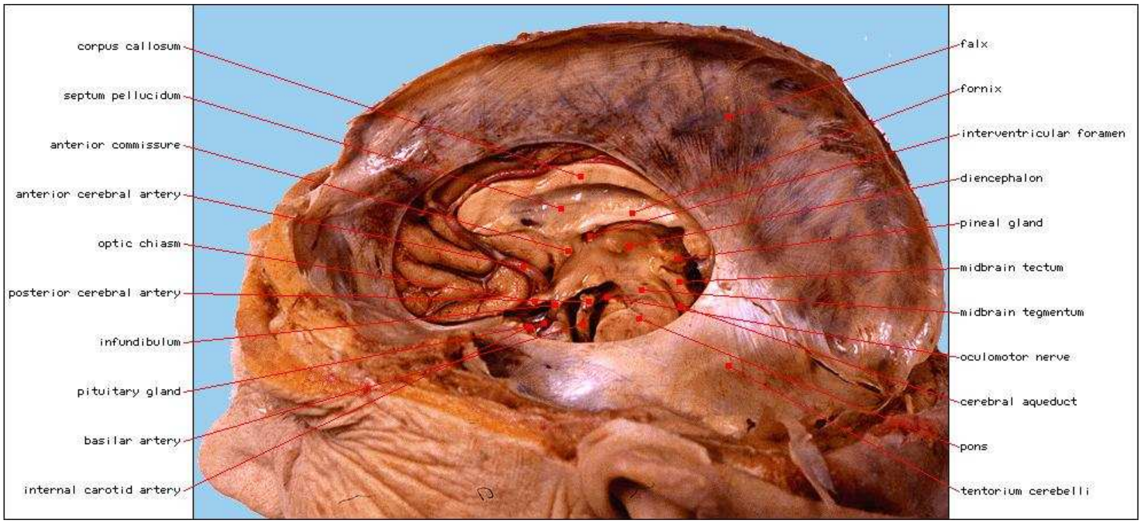

Figure 8.3: Falx cerebri

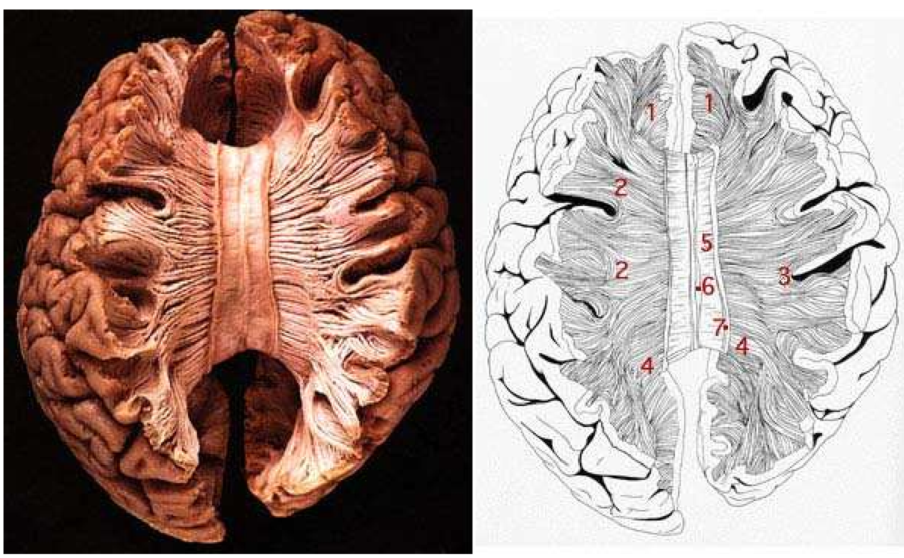

Figure 8.4: Corpus callosum : 1. Frontal forceps 2. Corpus callosum commissural fibers 3. Short arcuate fibers 4. Occipital forceps 5. Indusium griseum 6. Medial longitudinal stria 7. Lateral longitudinal stria

Bibliography

[1] Ferrant M, “Physics-based Deformable Modeling of Volumes and Surface for Medical Image Registration, Segmentation and Visualization”,PhD thesis, Louvain, Belgium: Universite Catholique de Louvain, 2001.

[2] Skrinjar O, “Deformable Models in Image-Guided Neurosurgery”, Thesis proposal, Avril 2002.

[3] Hagemann A, “A Biomechanical Model of the Human Head with Variable Material Properties for Intraoperative Image Correction”, PhD, 2001.

[4] Audette M, “Anatomical Suface Identification, Range-Sensing and Registration for Characterizing Intrasurgical Brain Deforamtions”, Thesis submission document, Octobre 2001.

[5] Nimsky Chet al, “Quantification of, Visualization of, and Compensation for Brain Shift Using Intraoperative Magnetic Resonance Imaging.” Neurosurgery 47:1070-1080, 2000

[6] Hill DLG et al, “Investigation of intraoperative brain deformation using a 1.5T interventional MR system: preliminary results.” IEEE Trans. Med. Imag 17:817-825 1998.

[7] Unia J, “Suivi Temporel de Structures Cérébrales dans des IRM à l’aide de modèles biomécaniques”, Rapport de DEA, ECL, 2001.

[8] Sébastien Ourselin. Recalage d’images médicales par appariement de régions - Application à la construction d’atlas histologiques 3D. Thèse de sciences, Université de Nice Sophia-Antipolis, January 2002.

[9] Picinbono G, “Modèle Géométriques et Physiques pour la simulation d’interventions chirurgicales ” Thèse de l’université de Nice, Fevrier 2001.

[10] Azar F, “Methods for Modeling and Predicting Mechanical Deformations of the Breast under External Perturbations”, Journal of Medical Image Analysis, January 2002.

[11] M. I. Miga et al, “Model-updated image guidance: Initial clinical experience with gravity-induced brain deformation”, IEEE Trans. on Med. Imaging, Vol. 18, No. 10, pp. 866-874, 1999.

[12] R. Comeau, A. Sadikot, A. Fenster et al. “Intraoperative Ultrasound for Guidance and Tissue Shift Correction in Image-Guided Neurosurgery.” Med. Phys. 27(4), pp. 787800, 2000.

[13] Miga MI, Paulsen KD, Hoopes PJ, Kennedy FE, Hartov A, Roberts DW. “In vivo modeling of interstitial pressure in the brain under surgical load using finite elements.” Journal of Biomechanical Engineering 122:354-363, 2000.

[14] M. I. Miga, K. D. Paulsen, F. E. Kennedy, A. Hartov, D. W. Roberts, ’Model-updated image-guided neurosurgery using the finite element method: Incorporation of the falx cerebri’, Lec. Notes in Comp. Sci. for 2nd Int. Conf. on MICCAI, Vol. 1679, pp. 900-909, 1999.

[15] C. Davatzikos, D. Shen, A. Mohamed, and S. Kyriacou, “A Framework for Predictive Modeling of Anatomical Deformations”, IEEE Trans. on Med. Imaging,20(8):836-843, 2001.

[16] Miller K., Chinzei K., Orssengo G. and Bednarz P. , “Mechanical properties of brain tissue in-vivo: experiment and computer simulation”, J. Biomechanics, Vol. 33, pp. 1369-1376, 2000

[17] Miller, K. and Chinzei, K., "Modeling of Brain Tissue Mechanical Properties; Bi-Phasic Versus Single-Phase Approach," in J. Middleton, M. L. Jones, and G.N. Pande (eds.) Computer Methods in Biomechanics & Biomedical Engineering, Gordon and Breach Science Publishers, The Netherlands, pp. 535-542, 1998.

[18] A. Castellano-Smith, D. L. G. Hill et al. “Constructing Patient Specific Models for Correcting Intraoperative Brain Deformation.” MICCAI 2001, Utrecht, NL

[19] A. Castellano-Smith, Thomas Hartkens, Julia A Schnabel, Rodney Hose, Haiying Liu, Walter Hall, Charles Truwit, David J Hawkes, Derek LG Hill “A Registration Based Mesh Construction Technique for Finite Element Models of Brains.” In Proc. SPIE Medical Imaging 2002, San Diego, California.

[20] Michael I. Miga, Ph.D.; David W. Roberts, M.D.; Francis E. Kennedy, Ph.D.; Leah A. Platenik, B.S.; Alex Hartov, Ph.D.; Karen E. Lunn, A.B.; Keith D. Paulsen, Ph.D. “Modeling of Retraction and Resection for Intraoperative Updating of Images. ” Neurosurgery 49: 75-85, 2001

[21] J.F.Mangin, V.Frouin, I.Bloch, J. Regis, J.Lopez Krahe, From 3D magnetic resonance images to structural representations of the cortex topography using topology preserving deformations, Journal of Mathematical Imaging and Vision, Vol. 5, pp 297-318, 1995

[22] Thirion, J.-P."Non-Rigid Matching using Demons" Computer Vision and Pattern Recognition, June CVPR96. San Francisco, California, USA

[23] Pascal Cachier. Recalage non rigide d’images médicales volumiques - contribution aux approches iconiques et géométriques. Thèse de sciences, École Centrale des Arts et Manufactures,PhD thesis, January 2002.

[24] A. Roche, G. Malandain, and N. Ayache. Unifying Maximum Likelihood Approaches in Medical Image Registration. International Journal of Imaging Systems and Technology: Special Issue on 3D Imaging, 11(1):71-80, 2000.

[25] Alexis Roche. Recalage d'images médicales par inférence statistique. Thèse de sciences, Université de Nice Sophia-Antipolis, February 2001.

[26] Ron Kikinis, Martha Elizabeth Shenton, Dan V. Iosifescu, Robert W. McCarley, Pairash Saiviroonporn, Hiroto H. Hokama, Andre Robatino, David Metcalf, Cindy Wible, Chiara M. Portas, Robert M. Donnino, Ferenc A. Jolesz: A Digital Brain Atlas for Surgical Planning, Model-Driven Segmentation, and Teaching. IEEE Transactions on Visualization and Computer Graphics 2(3): 232-241 (1996)

[27] R. Szeliski. Bayesian Modeling of Uncertainty in Low-Level Vision. *Int. J.of Comp. Vision*, 5(3):271 – 301, December 1990.